CHALMERS

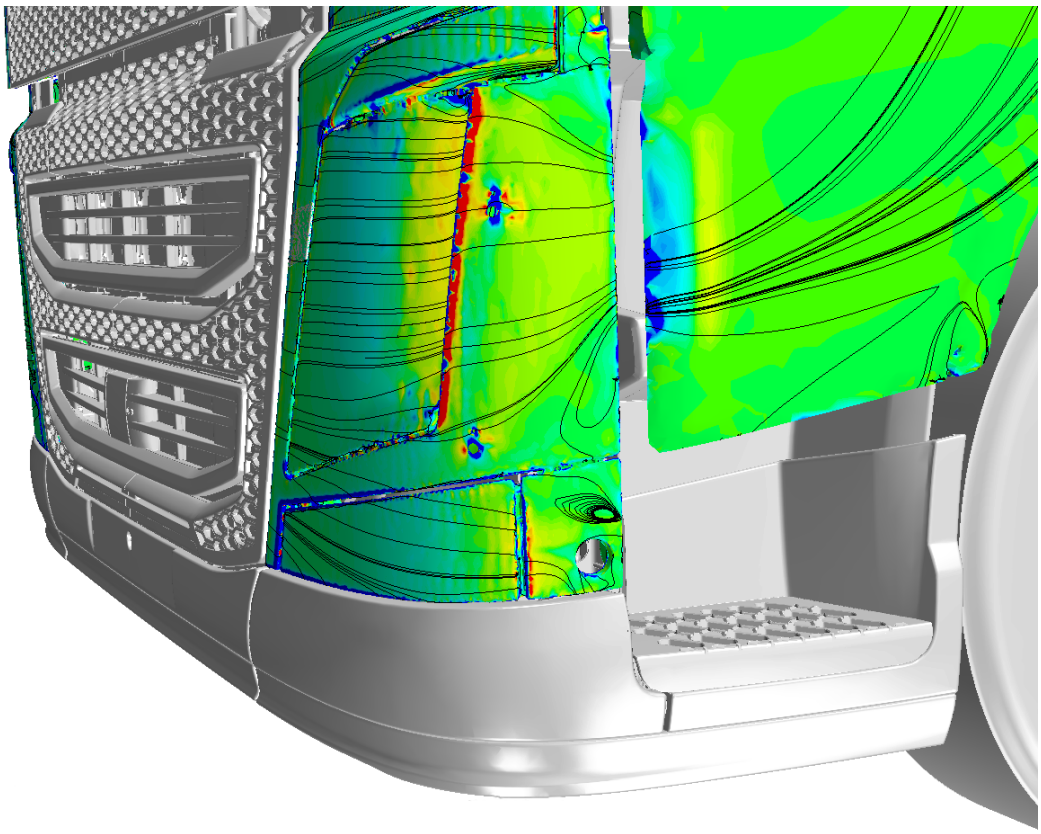

Investigation of Flow Separation around the Front Corners of a Truck using CFD

Master's thesis in Applied Mechanics

EMMA ELOFSSON

Department of Applied Mechanics
CHALMERS UNIVERSITY OF TECHNOLOGY
Gothenburg, Sweden, 2014
Master's thesis 2014:72

MASTER'S THESIS IN APPLIED MECHANICS

Investigation of Flow Separation around the Front Corners of a Truck using CFD

EMMA ELOFSSON

Department of Applied Mechanics
CHALMERS UNIVERSITY OF TECHNOLOGY
Gothenburg, Sweden, 2014

Investigation of Flow Separation around the Front Corners of a Truck using CFD
EMMA ELOFSSON

Master's thesis 2014:72
ISSN 1652-8557
Department of Applied Mechanics
Chalmers University of Technology
SE-412 96 Gothenburg
Sweden
Telephone +46 (0)31-772 1000

Cover: Local streamwise pressure gradient around the front corner of a Volvo FH16 truck.

Chalmers Reproservice
Gothenburg, Sweden 2014

Investigation of Flow Separation around the Front Corners of a Truck using CFD
EMMA ELOFSSON
Department of Applied Mechanics
Chalmers University of Technology

Abstract

Fuel consumption becomes more and more important for heavy duty vehicles. The increased fuel prices and the more restrictive legislations have pushed the development towards fuel efficient vehicles. The aerodynamic drag is a large contributor to the overall losses. The flow around the front corners of a truck is crucial since flow separation occurs there, which affects the overall flow and drag.

It is difficult to predict the flow separation point at a rounded corner. Therefore, the purpose of this thesis work is to provide Volvo Group Truck Technology with knowledge about what influences the flow separation on the front corners of the truck. Focus is also put on investigating how the separation is affected by the manner of how the flow is simulated.

In this investigation details are removed from the lower front of a Volvo FH16 truck. Removing details will affect the flow, but the assumption is that the behavior of the flow and the flow separation will be more apparent. A simplified model of the lower front was developed in a manner such that one geometrical feature of the front corner could be changed without affecting any other geometry. The geometrical features evaluated are the front corner radius between 80–300 mm and the following draft angle of either 0° or 12°. There were two main requirements when designing the simplified model. The first one was that the geometry and flow situation should be close to reality and the second requirement was that the front corner radius should be adjustable between at least 100–300 mm.

In this thesis CFD has been used to solve the flow with a mesh distribution mainly consistent of hexahedrals. The simulations have been carried out in STAR-CCM+. To model the turbulent flow, standard k–ε model with realizable coefficient and two-layer all y^+ wall treatment has been used.

The hypothesis was that there would be no significant difference in the simulation results for values of y^+ between 30–100. This has been shown not to be true for small radii where flow separation occurs. For a front corner radius smaller than 150 mm it was shown that the results deviated significant for meshes of $y^+ \approx 30$ compared to meshes of $y^+ \approx 60$, given that flow separation occurred. Therefore, it is recommended to have $y^+ \approx 1$ for areas consisting of small radii.

It has also been found that for a three-dimensional flow the flow separation point is not connected to a maximum value of the local streamwise pressure gradient, but it seems to be connected to the positive second derivative.

Using the simplified model with a draft angle of 12° resulted in an overall longer distance between the end of the corner arc and the gap just before the door. To vary the front corner radius has less impact on the drag with a draft angle of 12°. Both due to the smaller turn around the front corner which prohibits flow separation and the longer distance.

Keywords: Aerodynamics, Flow separation, Drag coefficient, CFD, Truck

Acknowledgements

The author of this master thesis, Emma Elofsson, would like to acknowledge some key persons who have guided and supported though the project.

First and foremost I would like to thank my industrial supervisor PhD Zenitha Chroneér for advising and supporting through out the project time. Many thanks for giving me the opportunity to carry out such an interesting thesis work in the industry. I also would like to thank Professor Lars Davidson for being my examiner.

Furthermore, I would like to thank Anders Tenstam for all advice and help regarding the project and CFD software support. Thanks also to Fredrik Ekeroth for help with CFD software support.

A special thanks to my friend Johanna Risö for being supportive and believing in me and last but not least, thanks to my family for their support and shown interest in my thesis work.

Nomenclature

Roman Capital Letters

A	vehicle frontal area [m^2]
C_D	drag coefficient
$C_{D,press}$	pressure drag contribution to drag coefficient
$C_{D,fric}$	friction drag contribution to drag coefficient
C_P	pressure coefficient
F_D	drag force [N]
L	reference length [m]
LSPG	local streamwise pressure gradient [N/m^3]
Re	Reynolds number
Re_d	Reynolds number based on diameter
Re_x	local Reynolds number for a flat plate
U	reference velocity [m/s]
U_a	air speed [m/s]
U_∞	free-stream velocity [m/s]
X	global longitudinal position [m]
Y	global lateral position [m]
Z	global vertical position [m]

Roman Small Letters

k	turbulent kinetic energy [m^2/s^2]
ℓ_0	large turbulent length scale [m]
ℓ_η	Kolmogorov length scale [m]
p	pressure [Pa]
p_{tot}	total pressure [Pa]
p_0	stagnation pressure [Pa]
p_∞	free-stream pressure [Pa]
t	time [s]
u_0	large turbulent velocity scale [m/s]
u_i, u_j	instantaneous velocities in x_i- resp. x_j-direction [m/s]
$\overline{u_i}$	mean of instantaneous velocity vector [m/s]
u^*	friction velocity [m/s]
x	longitudinal position on a flat plate measured from its leading edge [m]
x_i, x_j	vectors containing the global coordinates: (X, Y, Z) [m]
x_n	coordinate normal to wall [m]
x_s	coordinate parallel to wall [m]
y	wall-normal distance [m]
y^+	dimensionless wall distance
y^+_{low}	mesh with a distribution of $y^+ \approx 1$
$y^+_{low,c}$	y^+_{low} at the front corners and y^+_{high} at the other parts
y^+_{high}	mesh with a distribution of $y^+ \approx 30 - 100$

Greek Letters

α	draft angle [°]
α_0	draft angle of 0 [°]
α_{12}	draft angle of 12 [°]
δ	boundary layer thickness [m]
δ_{ij}	Kronecker's delta
ϵ	turbulent dissipation [m^2/s^3]
μ	laminar dynamic viscosity [kg/ms]
μ_T	turbulent dynamic viscosity [kg/ms]
ν	laminar kinematic viscosity [m^2/s]
ν_T	turbulent kinematic viscosity [m^2/s]
ρ	density of air [kg/m^3]
τ	shear stress [Pa]
τ_{ij}	Reynolds stress tensor [Pa]
τ_w	wall shear stress [Pa]

Abbreviations

CAD	Computed Aided Design
CFD	Computational Fluid Dynamics
DNS	Direct Numerical Simulation
LES	Large Eddy Simulation
LHS	Left Hand Side
LSPG	Local Streamwise Pressure Gradient
RANS	Reynolds-Averaged Navier-Stoke

Contents

1 Introduction

This section aims to introduce the reader in the aerodynamic field and the problems associated. The purpose as well as the scope and the objectives of this master thesis are presented in this section.

1.1 Background

Fuel consumption becomes more and more important for heavy duty vehicles. The increased fuel prices have pushed the development towards fuel efficient vehicles. For the future the increased fuel price together with regulations on CO_2 emissions will push the development even more towards efficient transports. The aerodynamic drag is a large contributor to the overall losses, especially at higher speeds. The flow around the front corners of a truck is very crucial to the overall flow and drag. If the flow separation here does not get predicted correctly, the flow between the cab and trailer will be affected and therefore the flow around the trailer. This can have significant impact on the overall drag.

Even though CFD (Computational Fluid Dynamics) has been used in the automotive business for the last two decades, there are still questions about the accuracy of the simulations. One area of particular interest is the point where the flow separates. For very sharp edges, the point of separation is well defined and most CFD codes can predict it very well. But as the radius increases, the point of separation becomes more difficult to predict.

When using CFD the position of the first cell in wall-normal direction is of great importance since it affects the flow results. The wall-normal distance is specified as the dimensionless wall distance, y^+.

1.2 Purpose

The purpose of this thesis work is to provide Volvo Group Truck Technology with knowledge about what influences the flow separation on the front corner of the truck. Focus is also put on investigating how the flow separation is affected by the manner of how the flow is simulated.

1.3 Objective

The aim of this project is to study how the flow separation changes for different radii of the front corners of a truck. To specify the purpose, the investigation of the flow separation has been divided into relevant objectives. These objectives are:

- Compare the effects of different geometrical features, front corner radii and draft angle, on the flow separation, i.e. compare the change in drag coefficient and flow field parameters.
- Investigate mesh dependence by changing mesh resolution using both high-y^+, $y^+ \approx 30 - 100$, and low-y^+, $y^+ \approx 1$, wall-treatment formulations.

1.4 Scope

The effects of different geometrical features will only be studied on a simplified model of the lower front. This since a simplified model will make it possible to change the front corners in a controlled way without changing any other geometry. The part of the front corner, including the headlamp, will be simplified to basic geometric shapes. The space just before the door will be simplified to a gap with a constant width and fixed on a longitudinal position. For a cross-section, the corner will be simplified to a circular arc with an adjustable radius and the distance between the end of arc and the gap will be simplified to a straight line. The angle between this straight line and the longitudinal direction is called draft angle.

Two parameters will be investigated: the front corner radius and the draft angle. This will be done using multiple front corner radii and two draft angles (0° and 12°). In the simplified model it should be possible to vary the radii between at least 100–300 mm.

Since there are no practical measurements available, the study will only result in numerical comparisons using CFD. The software STAR-CCM+ will be used with applied supplier-recommended settings as far as possible. Furthermore, only the recommended turbulence model will be used in all simulations and this model is the standard k–ε model with realizable coefficient and two-layer all y^+ wall treatment.

2 Geometry of a Volvo FH16 Truck

For this thesis, preexisting CAD models of a FH16 H2 tractor and a semi-trailer were given, where H2 refers to the height of the cab. This is shown in Figure 2.1. The parts of the truck of particular interest in this thesis are the ones in the lower front, which are colored in Figure 2.2. The group of parts is in this report considered as one unit and is referred to as the lower front.

Figure 2.1: CAD models of a FH16 H2 tractor with semi-trailer.

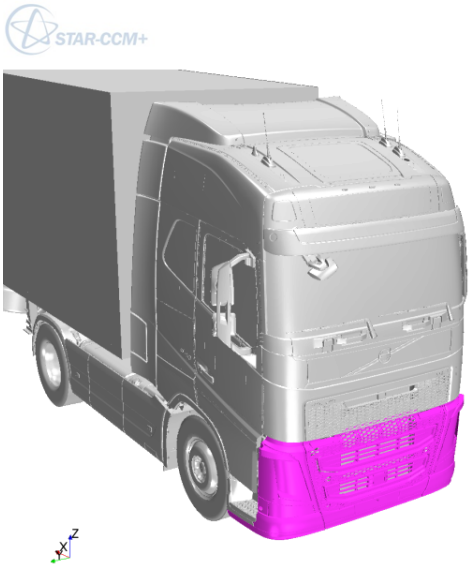

Figure 2.2: CAD model of a FH16 truck, wherein the lower front is marked with color.

The lower front consists of multiple parts, the most relevant for this thesis are named in Figure 2.3. Number 1–3 are parts of the headlamp and number 8 refers to the space between the lower front and the door, compare with Figure 2.2.

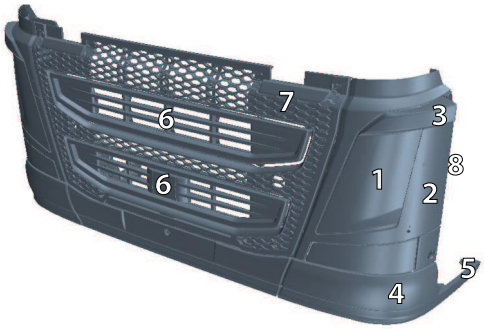

Figure 2.3: CAD model of complete lower front. 1: Headlamp lens, 2: Headlamp panel, 3: Side turn indicator, 4: Bumper, 5: Spoiler, 6: Foot step, 7: Lower front panel, 8: Gap.

3 Fluid Mechanics

Fluid mechanics is the study of fluids in either motion (fluid dynamics) or in rest (fluid statics). The dynamics of fluids satisfy a set of well-documented basic laws and solutions for theoretical examples can easily be obtained. However, theoretical solutions often rely on idealized examples and may not be available to practical applications. There are mainly two obstacles for solving the basic equations theoretically in practical flow situations, which are viscosity and complex geometry. The basic equations applied to any arbitrary geometry are too difficult to be solved theoretically, thus numerical computer techniques are required. Viscosity is another obstacle since it increases the difficulty of the basic equations and it has a destabilizing effect on all fluids, giving rise to disorderly and random phenomenon called turbulence. [1]

In this chapter the governing flow equations are presented as well as further explanation of the phenomenon known as turbulence.

3.1 Governing equations

The physics behind fluid mechanics can be described by three conservation laws: conservation of energy, conservation of mass and conservation of linear momentum. The conservation of mass and the conservation of linear momentum describe the motions of the fluid. From these laws the governing equations can be obtained. The governing equations under the assumption of an incompressible Newtonian viscous fluid with constant viscosity are given as:

$$\frac{\partial u_i}{\partial x_i} = 0 \tag{3.1}$$

$$\frac{\partial u_i}{\partial t} + u_j \frac{\partial u_i}{\partial x_j} = -\frac{1}{\rho}\frac{\partial p}{\partial x_i} + \nu \frac{\partial^2 u_i}{\partial x_j^2} \tag{3.2}$$

wherein the gravity is neglected, t is the time, p is the pressure, ν is the laminar kinematic viscosity, ρ is the density, u_i and u_j are the instantaneous velocities in x_i- resp. x_j-direction [2]. The coordinates (x_1, x_2, x_3) correspond to the global coordinates (X, Y, Z), which can be seen in Figure 2.2.

Equation 3.1 represents the continuity equation, i.e. the conservation of mass. The Navier-Stokes equations represent the conservation of linear momentum and are summarized in eq 3.2.

The most important parameter in fluid mechanics is the Reynolds number, Re, which is the dimensionless quantity obtained from the ratio of inertial and viscous forces. The Reynolds number is calculated as:

$$\mathrm{Re} = \frac{UL}{\nu} \tag{3.3}$$

where U is the reference velocity and L is the reference length. [1]

3.2 Turbulent Flow

There are two distinctive types of flows: laminar flow and turbulent flow. Laminar and turbulent flow types are properties of the flow and not of the fluid. In laminar flow the fluid flows smoothly with no turbulent perturbations and is characterized by shear layers sliding past each other, where the outer layers move faster than the inner ones and no mixing occurs. However, in turbulent flow the shear layers are mixed.

There is no exact definition of turbulent flow, but there are some properties to characterize this flow type. According to [3] and [4] some of these properties are:

- **Randomness and Irregularity**
  Turbulent flow is irregular, chaotic and has an unpredictable stochastic behavior.

- **Diffusivity**
  In turbulent flow the diffusivity increases, which causes rapid mixing and increased rates of momentum and heat transfer.

- **High Reynolds Number**
  Turbulent flow occurs at high Reynolds number.

- **Three-Dimensional and Rotational**
  Turbulent flow is always three-dimensional and unsteady. It is always three-dimensional since turbulence contains vorticity, which physically means rotation of a fluid particle. The random vorticity fluctuations that characterize the turbulent flows are maintained by the three-dimensional mechanisms: vortex stretching and vortex tilting, which are absent in two-dimensional flows.

- **Dissipation**
  Turbulent flow is dissipative. The concept of eddies (rotational structures) are essential in the explanation of transfer of kinetic energy. An eddy has a characteristic length and velocity, which are called length and velocity scales. The transfer process is explained as follows: the largest eddies extract their kinetic energy from the mean flow and their length scale, ℓ_0, is of the same order as the flow geometry (e.g. boundary layer thickness). The larger eddies pass on their kinetic energy to slightly smaller eddies, during one revolution, which in turn transfer their kinetic energy to even smaller eddies. Eventually the smallest eddies are reached and dissipation takes place, meaning that the kinetic energy in the smallest eddies are transformed into thermal energy (heat). The smallest eddies are isotropic and referred to as Kolmogorov scales. The Kolmogorov length scale is denoted ℓ_η.

3.3 Boundary Layers

When an air flow enters a surface with friction, (i.e. the velocities at the wall is zero) the friction drag between the layers of the air flow and the surface creates a velocity gradient, which means that the outer layers move faster than the inner ones. The air movement causes a boundary layer to develop on the surface and the boundary layer thickness, δ, grows across the surface. δ is defined as the distance away from the surface where the velocity parallel to the surface has reached 99 % of the free-stream velocity, U_∞. [2]

For high Reynolds numbers the boundary layer is a very thin layer close to the surface. Initially, as a flow enters a surface the boundary layer is laminar, but as traveling along the surface the flow becomes turbulent [1]. A simple case of the surface is a flat plate. The position on the plate, measured from the leading edge, is referred to as x. Please see Figure 3.1.

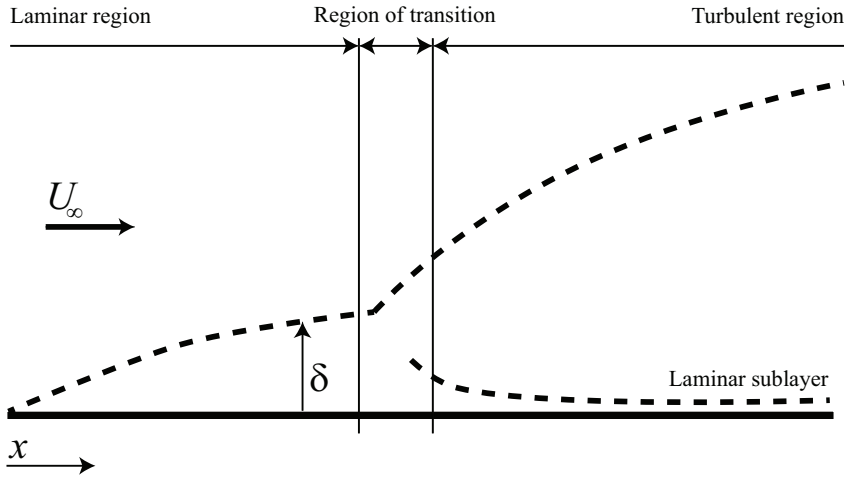

Figure 3.1: Boundary layer growth on a flat plate for high Re. [2]

Depending on the flow type and the shape of the geometry, different δ will be obtained. According to [5] the approximated relations of δ for a flat plate are formulated as:

$$\delta = \frac{5x}{\sqrt{\mathrm{Re}_x}} \tag{3.4}$$

$$\delta = \frac{0.385x}{\sqrt[5]{\mathrm{Re}_x}} \tag{3.5}$$

where eq 3.4 gives the relation between the boundary layer growth and x for a laminar flow and eq 3.5 gives this relation for a turbulent flow.

There exists a region where the boundary layer may be either laminar or turbulent and fluctuations between these flow types occur. This area is called the region of transition. Further downstream of this region, for a certain value of x, the flow of the boundary layer will remain turbulent.

The local Reynolds number of the flow along the surface of the flat plate, Re_x, gives an indication whether the boundary layer is expected to be laminar or turbulent. Laminar flow, wherein large velocity gradients exist, is dominated by viscous forces and is known to only exist at low Reynolds number. For increasing x the flow eventually reaches the region of transition. Until this region is reached Re_x increases with increased x according to eq. 3.4.

For a flat plate the region of transition is reached when $\mathrm{Re}_x \approx 500\ 000$ [3]. The transition, however, is greatly dependent on the perturbations of the outer flow. If the outer flow is smooth the transition may be delayed until $\mathrm{Re}_x \approx 3\ 000\ 000$, but when the outer flow experience strong perturbations the transition may even occur when $\mathrm{Re}_x \approx 200\ 000$ [2].

The turbulent boundary layer consists of the viscous sublayer, the logarithmic region and the buffer region.

The sublayer is the thin film of fluid close to the wall where the flow still is laminar. The location of these regions can be related to the dimensionless wall distance, y^+, (for definition see section 5.2) and they are always located at the same y^+. The viscous sublayer occurs at $y^+ \leq 5$, the buffer region is located at $5 < y^+ < 30$ and the logarithmic region occurs at $30 \leq y^+$.

Schematic illustration of the boundary layer on a flat plate for high-Re flows is shown in Figure 3.1.

4 Aerodynamics

This section gives an introduction to aerodynamics, including aerodynamic forces and flow separation. The relation between air speed and pressure is also included as well as an introduction to the aerodynamics of a truck.

4.1 Connection between Air Speed and Pressure

For incompressible steady flows, the Bernoulli equation relates air speed, U_a, to the pressure as:

$$p + \frac{1}{2}\rho U_a^2 = constant \tag{4.1}$$

wherein the difference in height has been ignored [6]. In addition to the restrictions mentioned above the Bernoulli equation is only valid for frictionless flow along a streamline. Thus, this equation is not valid in boundary layers and different streamlines may have different constants.

From eq 4.1 it can be seen that an increased pressure gives a decreased speed at the same position and vice versa. From this equation it can also be seen that at any point where the air flow is decelerated to zero velocity, due to an obstacle, the pressure reaches its maximum value, which is referred to as the stagnation pressure, p_0. Further, the second term in eq 4.1 is called the dynamic pressure, which represents the kinetic energy of a unit volume.

4.2 Aerodynamic Forces

The forces on a body due to the flow consist of pressure and shear forces. The aerodynamic drag force, F_D, is the component of the overall forces which is parallel to the free-stream direction, i.e. the drag consists of pressure drag and friction drag. The pressure drag is the force acting normal to the surface and is due to a pressure difference between the front and the rear of the body. The friction drag, however, is acting tangential to surface and is caused by shear stresses between fluid and surface.

4.2.1 Pressure Coefficient

The difference between the pressure at any point and the pressure of the free-stream, p_∞, (i.e. the reference pressure) is directly dependent on the dynamic pressure. The pressure coefficient, C_p, defines this relation as:

$$C_p = \frac{p - p_\infty}{\frac{1}{2}\rho U_\infty^2} \tag{4.2}$$

where U_∞ is the free-stream velocity [1]. Theoretically the maximal value of C_p is 1 for incompressible flow, which corresponds to p_0.

4.2.2 Drag Coefficient

The drag coefficient, C_D, is defined as:

$$C_D = \frac{F_D}{\frac{1}{2}\rho U_\infty^2 A} \tag{4.3}$$

where A is the frontal area [6]. As mentioned in section 4.2, both pressure drag and friction drag contribute to F_D. Thus, C_D may be expressed as:

$$C_D = C_{D,press} + C_{D,fric} \tag{4.4}$$

where the relative contribution depends on the shape of the body, especially its thickness. A flat plate of zero thickness exists of 100% friction drag, but at thickness equal to the chord length the pressure drag contributes with almost 97%. [1]

4.3 Flow Separation

Flow separation is a large contributor to the aerodynamic drag. This phenomenon is caused by excessive momentum loss near the surface in a boundary layer when the flow is trying to move against an increased pressure. Flow separation is present for flow situations involving blunt bodies. In this section the basic knowledge of flow separation will be described.

As an air flow approaches a blunt body the flow decelerates and the pressure increases until the air flow reaches the point just in front of the body, see point A in Figure 4.1. Point A is a so called stagnation point, i.e. the flow has decelerated to zero velocity and the pressure is equal to p_0. Further, when the flow reaches point B, the pressure is low and the pressure difference between point A and point B will accelerate the flow until point B is reached. After point B, the pressure gradually rises again as the flow decelerates. Thus, the flow has to travel from low to high pressure which is done by slowing down and losing some kinetic energy. [6]

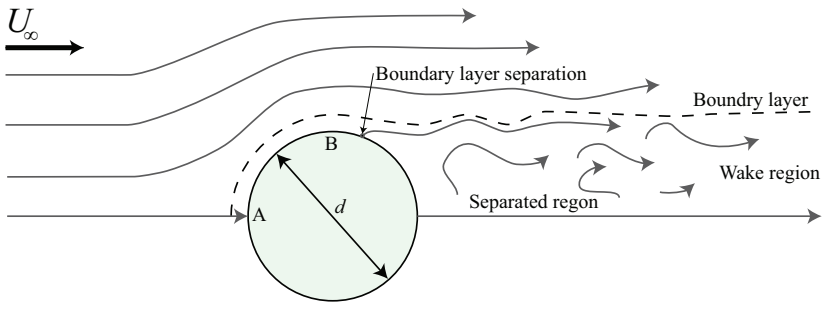

Figure 4.1: Turbulent boundary layer flow around a circular body, $\mathrm{Re}_d \approx 2 \times 10^5$. A: Stagnation point, B: low pressure point (point on the corner crest). [7]

Some energy is lost due to friction which is dissipated close to the surface. In the region between point A and point B, the negative pressure gradient acts as a counterpart to the retarding effect of the shear stress (which is due to viscosity), but in the region where the positive pressure gradient acts they cooperate. Most affected is the region close to the wall where the momentum is lower than in the region near the free stream. [6]

If the pressure gradually increases the process of turbulent mixing or molecular impact allows the outer layers to pull the inner ones along. Energy from the faster moving fluid is fed in towards the surface. If the rate increase of pressure is too great, the mixing process will be too slow to keep the lower part of the layer moving. When this happens the boundary layer stops following the contours of the surface and separates away. [6], [8]

If and where a flow separation on a circular cylinder occurs is highly dependent on the Reynolds number based on the diameter, Re_d. When Re_d is above 10^4 the flow can be divided into at least four different regimes which are subcritical, critical, supercritical and transcritical. The subcritical regime occurs below $\mathrm{Re}_d \approx 2{\times}10^5$ and in this regime the boundary layers separates in a laminar state at about 80° from the forward stagnation point. For higher Re_d the critical regime is reached and the boundary layer separates in a turbulent state, which delays the separation until about 120° from the forward stagnation point (Point A in Figure 4.1 is a forward stagnation point). [8], [9]

4.4 Favorable and Unfavorable Pressure

As mentioned in section 4.3, flow separation tends to occur when the air flow travels from low to high pressure, which is known as an adverse pressure gradient. Consequently, flow traveling from high to low pressure is referred to as a favorable pressure gradient. A favorable pressure gradient inhibits flow separation, slows down the rate of boundary layer growth and delays the transition from laminar to turbulent flow. Thus, the pressure gradient plays a great role in flow separation, which can be explained by geometrical arguments about the second derivative of the velocity at the wall.

From linear momentum equation (eq 3.2), considering steady two-dimensional incompressible viscous flows, applying no-slip condition at the wall and neglecting gravity, following relation is obtained:

$$\left.\frac{\partial \tau}{\partial x_n}\right|_{wall} = \mu \left.\frac{\partial^2 u_s}{\partial x_n^2}\right|_{wall} = \frac{dp}{dx_s} \tag{4.5}$$

where τ is the shear stress, x_s is the direction along the wall and x_n is the direction normal to the wall [1]. The relation in eq 4.5 can be applied to a curved wall if the radius of its curvature is large compared with the boundary layer thickness. The equation holds for both turbulent and laminar boundary layers.

From eq. 4.5 it is seen that for an adverse pressure gradient, $\partial^2 u_s/\partial x_n^2$ is positive at the wall. However, this term must take a negative value at the outer layer in order to the boundary layer to be able to merge smoothly with the free stream, which it necessary. Hence, somewhere in the boundary layer there must be an inflection point where $\partial^2 u_s/\partial x_n^2$ takes the value of zero. [1]

For a weak adverse pressure gradient the flow does not separate but it is vulnerable to transition to turbulent flow. For a critical adverse pressure gradient flow separation occurs. This is when $\partial u_s/\partial x_n = 0$ at the wall, which is equivalent to zero wall shear stress, $\tau_w = 0$. Any stronger adverse pressure gradient will cause backflow at the wall. [2]

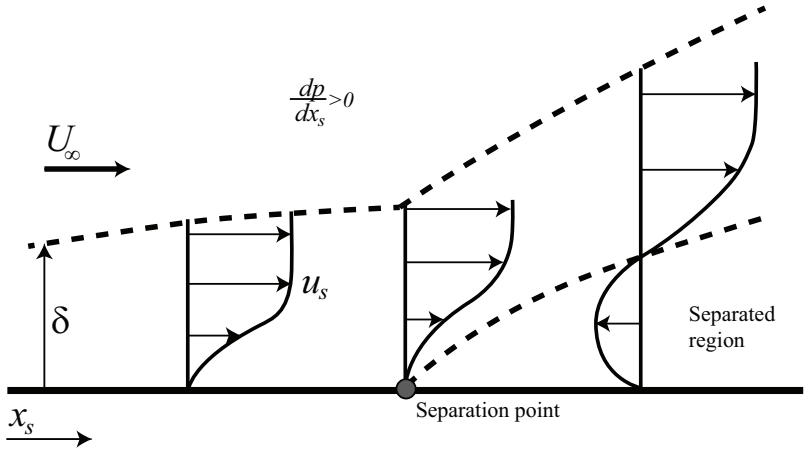

Figure 4.2: Velocity profiles in boundary layer facing an unfavorable pressure gradient. [2]

Overall, in order to the flow to separate, u_s adjacent to the wall must be zero or negative. A positive pressure gradient is a necessary condition for flow separation but the flow can remain unseparated with an adverse pressure gradient. The pressure variation is not the only factor influencing the separation. The type of boundary layer and its thickness influence the friction drag and the flow separation. A turbulent boundary layer resists separation better than a laminar boundary layer. This since a turbulent boundary layer has both greater momentum and energy, which permit it to remain unseparated for a greater distance in the presence of an adverse pressure gradient.

A schematic illustration of a separated boundary layer can be found in Figure 4.2.

4.5 Truck Aerodynamics

In fluid mechanics point of view, trucks are blunt bodies close to the ground. The flow over a truck is extremely complex and fully three-dimensional due to detailed geometry close to the ground and rotating wheels. The effect of separation and reattachment dominates most of the ground vehicles surface region. [6]

Since the flow is highly three-dimensional, the formulation of the boundary layer is much more complicated including a cross-stream velocity. Therefore, the simple criterion for the separation point obtained by using a two-dimensional flow approximation, $\tau_w = 0$, is not applicable. However, the local streamwise pressure gradient (LSPG) is still important since it affects if and where separation occurs. The local streamwise pressure gradient is calculated as the dot product between the pressure gradient vector, dp/dx_i, and the normalized instantaneous velocity vector, $u_i/|u_j|$, as:

$$\text{LSPG} = \frac{dp}{dx_i} \cdot \frac{u_i}{|u_j|} \tag{4.6}$$

Road vehicles operate normally in Reynolds number region in excess of 10^6 [10]. For most road vehicles, the transition to turbulent boundary layer takes place after not more than about 30 mm from the front of the vehicle. [6]

The flow passing road vehicle contains steep pressure gradients and large regions of separated flow [10]. Separation normally occurs where the resultant flow encounters a sharp edge. There are larger areas of separated flow which occur at the A-pillars, at the rear of the vehicle, underneath the vehicle and around the wheel region. There are also smaller areas of separated flow which occur around attached component such as headlights, mirrors, door handles and windshield wipers. In this thesis focus lies in flow separation caused by the front corners.

5 Computational Fluid Dynamics

This section includes theory to approximately solve the flow. This is done by dividing the simulation area into cells in which the flow equations are numerically solved. The cell distribution can be done in several ways and different distributions are suitable for different simulation cases.

5.1 Mesh Theory

To solve the flow equations numerically the computational domain is discretized into cells which form a grid. The cells can be shaped as tetrahedral, hexahedral or polyhedral elements. Which one of these to use depends on the geometry and flow characteristics.

The grid has significant impact on convergence, solution accuracy and CPU time required. For external aerodynamic flow simulations with a predominate stream direction, a mesh consistent of hexahedral cells with prism layers is preferred. This since it is faster to generate, require less memory and gives faster convergence compared to the polyhedral mesh. [11]

The accuracy of the mesh is of great importance to receive adequate and mesh independent solutions. The mesh density should be high enough to capture all relevant flow features and the mesh adjacent to the wall should be fine enough to resolve the flow of the boundary layer (where the velocity gradients are steepest). The use of prism layers allows a denser mesh in wall-normal direction close to the wall in order to solve the flow accurately. This is critical in determining flow features such as flow separation. If needed, the use of prism layer gives the possibility to fully resolve the viscous sublayer. Wall functions may be used if it is not critical to fully resolve the viscous sublayer. [3], [11]

The shape of the element as well as the quality of the mesh contributes to the accuracy of the solution. For the same cell count, hexahedral meshes will give more accurate solutions than tetrahedral, especially if the grid lines are aligned with the flow.

Skewness, smoothness and aspect ratio are three indicators of the quality of the mesh. The parameter skewness indicates how close to ideal a cell is. Highly skewed faces are unacceptable since the equations being solved assume relatively equiangular cells. A good quality grid has a value of approximately 0.4 or less. The quality measurement smoothness aims to indicate sudden large changes in the mesh. The change in cell size should be gradual and smooth. Ideally, the maximum change in grid space should be less than 1.2.

Aspect ratio describes the ratio of the longest edge length to shortest edge length. To solve relevant flow features adequately where the flow is multidimensional, the cell aspect ratio should be near one and the change in cell size should be smooth. The use of prism layers allows high aspect ratios. Consequently, better cross-stream resolution is possible without introducing an excessive streamwise resolution.

5.2 Dimensionless Wall Distance

The dimensionless wall distance, y^+, is defined as:

$$y^+ = \frac{u^* y}{\nu} \tag{5.1}$$

where y is the distance normal to the wall and $u^* = \sqrt{\tau_w/\rho}$ is the friction velocity.

5.3 Software

STAR-CCM+ is a CAE software developed by CD-adapco. It is an engineering program for solving problems involving flow (of fluids or solids), heat transfer and stress. [11]

To simplify the use of the program there are manly two guides available for this thesis. The first one is a general guide from CD-adapco available for all users. The second one is more detailed and has been developed in cooperation with Volvo GTT, which specifies the best settings with regard to good solutions, stability and consumption of CPU time.

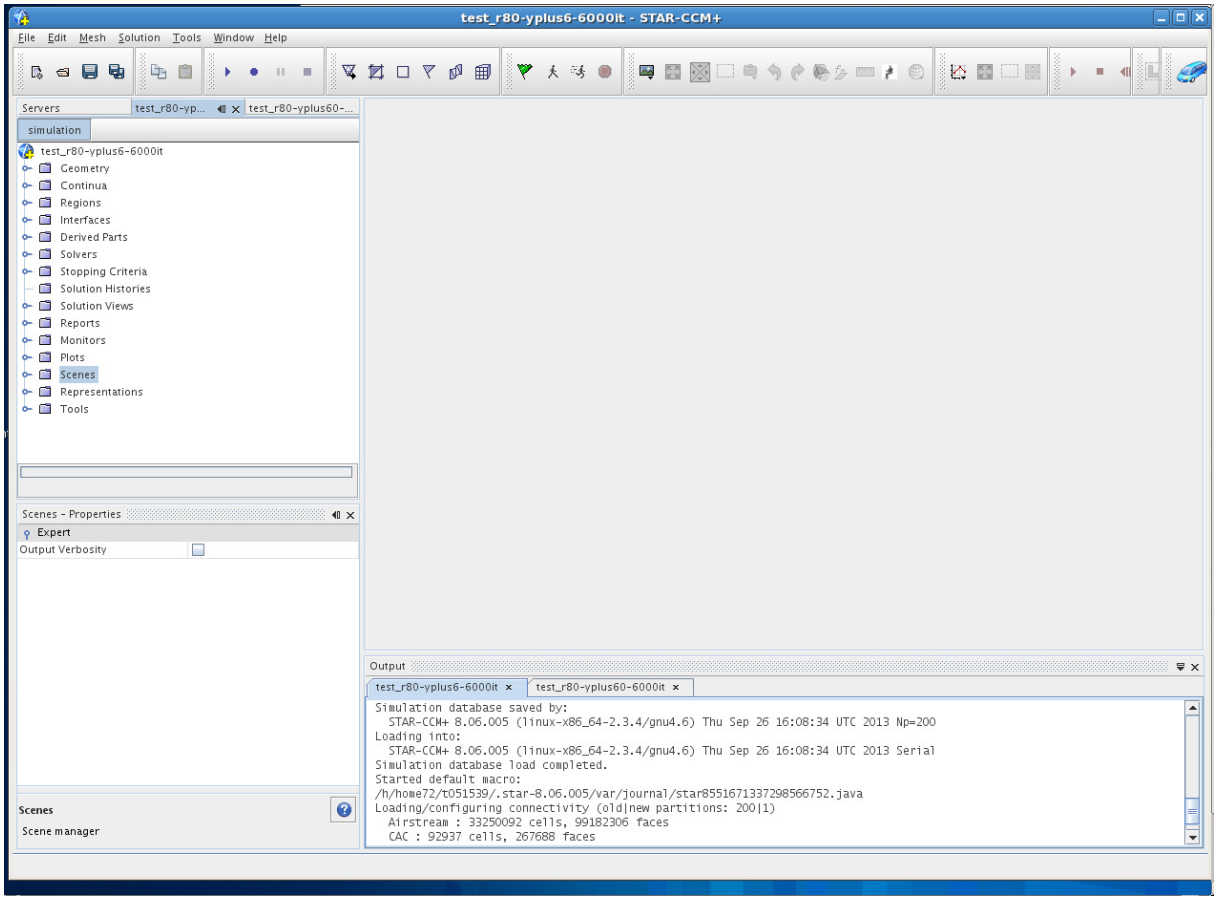

Figure 5.1: STAR-CCM+ interface.

When starting a new case an empty three structure are created. In the *Geometry* folder either external CAD parts can be imported or created using a built-in design function.

In STAR-CCM+, the mesh generation is done using an automatic mesh generator, which requires specification of mesh parameters (type of cells, cell sizes etc.) of the continuum as well as of the parts. The *Continua* folder contains all mesh continuum, where the general mesh settings for the continuum are set. This folder also contains all physic continuum, in which the physical properties of the continuum are set. The *Region* folder contains the parts of the geometry which will be included in the simulation. In this folder boundary conditions of the part surfaces are specified as well as the type of mesh, cell sizes and physical properties of the part surfaces. In the *Interface* folder, linked surfaces are connected. The surface are linked if, for instance, heat should be transferred though them. In the *Derived parts* folder, section cuts and points can be created to, among other things, enable visualization of simulation results.

5.3.1 Total Pressure

In STAR-CCM+, there are two predefined functions related to the total pressure. One is simply called the total pressure defined as: $p_{tot} = p + \frac{1}{2}\rho U_a^2$. The other one is called absolute total pressure which is the dynamic head, p_{ref}, added to p_{tot}. In this thesis, iso surface of p_{tot} will be used to visualize irreversible losses.

6 Turbulence Modeling

The most desirable numerical results are obtained from solving the Navies-Stokes equations completely without any simplifications. The method is called Direct Numerical Simulation (DNS) which requires a grid resolution fine enough to resolve the Kolmogorov scales of the flow. The enormous amount of cells required to directly solve the Navier–Stokes equations for turbulent flows are too computational expensive, except for simple low-Re flows. Thus, the DNS method is out of reach for industrial applications for today's computer capacity. Therefore simpler methods, i.e. approximations of the Navier–Stokes equations, are needed.

There are numerous turbulence models to approximate the physics of the turbulent flows. These models are mainly divided into models based on Reynolds-Averaged Navier–Stokes (RANS) equations, hybrid models, Large Eddy Simulation (LES) and DNS. This section will present some theory about the eddy-viscosity model based on RANS equations used in this thesis work.

6.1 Reynolds-Averaged Navier–Stokes

Turbulent flow is always unsteady and to resolve all turbulent scales requires very fine resolution in both space and time [3]. One approach of approximating the Navier–Stokes equations for turbulent flow is Reynolds averaging. The idea is to decompose the instantaneous variables, u_i and p, into a mean and a fluctuating value. E.g. u_i is decomposed into a mean value, $\overline{u}_i$, and a fluctuating value, u_i', as:

$$u_i = \overline{u}_i + u_i' \tag{6.1}$$

By inserting the decomposed relations into the incompressible Navier–Stokes equations (eq 3.2) and then perform Reynolds averaging, the RANS equations are obtained to:

$$\rho\overline{u}_i\frac{\partial\overline{u}_j}{\partial x_i} = \frac{\partial}{\partial x_j}\left[-\delta_{ij}\overline{p} + \mu\left(\frac{\partial\overline{u}_i}{\partial x_j} + \frac{\partial\overline{u}_j}{\partial x_i}\right) - \rho\overline{u_i'u_j'}\right] \tag{6.2}$$

In this time-averaging process the transient term disappears and Reynolds stress tensor, denoted as $\tau_{ij} = -\rho\overline{u_i'u_j'}$, appears. The components of τ_{ij} are called Reynolds stresses, which describe the turbulent fluctuations' effect on the change in momentum of the fluid.

There are several types of turbulence models based on the RANS equations. The one used in this thesis is an eddy-viscosity model which aims to model τ_{ij} with a kinematic turbulent eddy viscosity, ν_t.

There are also numerous eddy-viscosity models, which differ in their way of computing the Reynolds stresses. RANS models of the first order follow the Boussinesq assumption.

6.2 Boussinesq Assumption

The Boussinesq assumption introduces the dynamic turbulent eddy viscosity, $\mu_t = \nu_t \rho$, to model the unknown Reynolds stresses. Unlike the laminar viscosity, the turbulent one depends on the flow and it is proportional to the product between the large turbulent velocity scale, u_0, and corresponding length scale as:

$$\mu_t \propto \rho u_0 \ell_0. \tag{6.3}$$

The assumption states that τ_{ij} is proportional to the mean strain-rate tensor, $\overline{S}_{ij}$, as follows:

$$\tau_{ij} = 2\mu_t \overline{S}_{ij} - \frac{2}{3}\rho k \delta_{ij} \tag{6.4}$$

where δ_{ij} is the Kronecker's delta and k is the turbulent kinetic energy [3].

When this assumption is introduced, there is a drastic simplification since six unknown Reynolds stresses are replaced by only one unknown. Its weakness is that it is not generally valid. There is nothing that says that τ_{ij} must be proportional to $\overline{S}_{ij}$, which is only true for simple flows. Therefore, models based on this assumption have problem predicting complex flows.

6.3 Standard k–ε Model

The standard k–ε model is a two-equation eddy-viscosity model involving the modeled transport equations for k and its dissipation, ε. This model focuses on the mechanisms that affect the turbulent kinetic energy. [12]

The modeled k equation is obtained from the exact equation of k, but the unknown terms: turbulent diffusion, production and buoyancy are modeled based on the Boussinesq assumption. The modeled ε equation is set up similar to the modeled k equation. [3]

The quantities k and ε are used to define the velocity and length scales in eq 6.3. Thus, ν_t is expressed as:

$$\nu_t = \frac{c_\mu k^2}{\epsilon} \tag{6.5}$$

This expression is only valid for high Reynolds numbers, where the rate at which the large eddies extract energy from the mean flow is precisely matched to the rate of transfer of energy across the energy spectrum to the small, dissipating, eddies. [12]

The main advantages of using the k–ε model are the relatively simple implementation (due to the use of an isotropic eddy viscosity), the robustness of the model and convergence is easily achieved. In addition, the model is not computational heavy and works reasonable well for a large number of engineering flows. [3]

The main drawbacks with this model are poor prediction for flows with strong streamline curvatures, highly swirl components, strong separations and irrotational strains (stagnation flows).

The poor prediction of these flows is due to the use of an isotropic eddy viscosity, which is the same in all directions. The production of k in regions with large strain rate (near a stagnation point) is over-predicted. In boundary layers approaching separation, the production due to normal stress is of the same magnitude as that due to shear stress and the shear stress is over-predicted in adverse pressure gradient regions.

As mentioned, k–ε model provides accurate solutions only for fully turbulent flows. A flow is not fully turbulent in a boundary layer and the viscous effects are significant here. Very steep gradients occur in a boundary layer, which cause the model to predict the near-wall behavior poorly. To improve the performance of the k–ε model in regions near the wall, implementation of either low-Re turbulence modeling or wall functions is required.

In STAR-CCM+, the implementation of the transport equations for k and ε has been done using the form by Jones and Launder with coefficients suggested by Launder and Sharma. [11]

6.4 Wall Treatment

In STAR-CCM+ the set of near-wall modeling assumptions for each turbulence model are referred to as wall treatment. There are three types of wall treatments provided:

- **Low-y^+ Wall Treatment**
  This wall treatment is consistent with low-Re turbulence models which employ a turbulence model that is valid throughout the entire turbulent boundary layer. It assumes that the viscous sublayer is completely resolved. Hence, a fine mesh with a distribution of $y^+ \approx 1$ is required. The use of this wall treatment may lead to significant computational cost, especially for high-Re flows. A mesh with a distribution of $y^+ \approx 1$ is henceforth abbreviated to y^+_{low}.

- **High-y^+ Wall Treatment**
  Known as the classical wall function approach, which assumes that the near-wall cell lies within the logarithmic region, i.e. $y^+ \approx 30 - 100$. Assumptions of the distribution of the flow close to the wall are made, which provide a lot of savings of the resolution near the wall. The main disadvantage of using the high-y^+ wall treatment is that the viscous-dominated region of the boundary layers is not resolved. A mesh with a distribution of $y^+ \approx 30 - 100$ is henceforth abbreviated to y^+_{high}.

- **All-y^+ Wall Treatment**
  This is a hybrid model, which mixes the low-y^+ and high-y^+ wall treatments. It is constructed to recover the other model's behavior in the limit of fine or coarse meshes. This wall treatment is designed to emulate the low-y^+ wall treatment for y^+_{low} and the high-y^+ wall treatment for y^+_{high}. The advantage of using all-y^+ wall treatment is the more realistic solutions for meshes in the intermediate area compared to both the other wall treatments. This wall treatment is recommended for most simulations. [11]

The profiles of the mean flow quantities in the near-wall region need to be specified in both high-y^+ and all-y^+ wall treatment. These profiles are called wall laws.

In STAR-CCM+ two different set of wall laws are implemented. The first set is the standard wall law which is often applied together with high-y^+. These wall laws describe the slope discontinuity between laminar and turbulent profiles. The second set of wall laws is called the blend wall law. This set is often applied on turbulence models using damping functions. The blend wall laws describe a buffer region that smoothly blends the laminar and turbulent profile together.

6.5 Two-Layer Approach

The two-layer approach is an alternative to the use of low-Re turbulence models. The method is based on the division of the computational domain, which is divided into two layers. In the layer next to the wall, ν_t and ε are described as functions of the wall distance. In the near-wall layer ε is blended smoothly with the computed values from the transport equation in the second layer. The equation of ν_t is computed in the entire flow.

The advantage with this approach is that the results are often as good as or better than using approaches with damping functions, which low-Re turbulence models often use. In STAR-CCM+, the two-layer formulations work with both y^+_{low} and y^+_{high}.

6.6 Two-Layer All y^+ Wall Treatment

In STAR-CCM+, the formulation of the equations for the two-layer all y^+ wall treatment is identical to the formulation for the all-y^+ wall treatment, but contains a wall boundary condition for ε consistent with the two-layer formulation.

6.7 Realizability Constraints

There are several realizability constraints. One of the most used ones is that the normal stresses should stay positive, i.e. $\overline{v_i'^2} \geq 0$ for all i. This criterion is of importance for eddy-viscosity models in stagnation flow. Another constraint is the Schwarz's inequality, which says that the correlation coefficient for the shear stress should not exceed one, i.e. $\frac{\overline{v_i' v_j'}}{\overline{v_i'^2}\,\overline{v_j'^2}} \leq 1$. [3], [13]

6.8 Realizable k–ε Model

This model is an improvement of the standard k–ε model, which obeys the realizability constraints mentioned earlier. The k equation is the same as the one used in standard k–ε model, but the transport equation for ε is new and improved.

The critical coefficient of the turbulent viscosity, C_μ, is expressed as a function of the mean flow and the turbulence properties, instead of being constant as in the standard model. The new variable C_μ is based on experimental observations and ensures the positivity of the normal stresses and Schwarz's inequality.

The realizable k–ε model is stantially better than the standard k–ε model for cases involving planar and round jets, boundary layers under strong adverse pressure gradients or separation, rotation and strong streamline curvature. The production of k is limited and thus better performance in stagnation flows. In other cases this model is atleast as good as the standard k–ε model. The main drawback with this model is the limitation due to the use of a eddy viscosity which is assumed to be isotropic.

6.9 Standard k–ε Model with Realizable Coefficient

The eddy-viscosity models over-predict the production of k in stagnation flows, which can affect the rest of the flow solution. To overcome this, a lower limit on the turbulence time scale, C_T, (realizable coefficient) can be applied on the eddy-viscosity formula to satisfy the realizability constraint of positive normal stresses. [11],[12].

In STAR-CCM+, the realizablie coefficient is applied to standard k–ε model through ν_t, which is computed as $\nu_t = C_\mu kT$ and where T is the turbulent time scale. T is computed as:

$$T = \begin{cases} \max(\frac{k}{\epsilon}, C_t\sqrt{\frac{\nu}{\epsilon}}), & \text{without realizability} \\ \min(\max(\frac{k}{\epsilon}, C_t\sqrt{\frac{\nu}{\epsilon}}, \frac{1}{C_T S})), & \text{with realizability} \end{cases} \tag{6.6}$$

where S is the modulus of the mean strain-rate tensor and the model coefficient $C_t = 1$.

7 Reference Model

The reference model was a Volvo truck which consisted of CAD models of a FH16 H2 tractor and a semi-trailer, shown in Figure 2.1. These CAD models were imported into the *Geometry* folder in STAR-CCM+. All parts of the geometry which will be considered in the calculations were assigned to a region. A physics continua along with a mesh continua were created for each fluid continuum and applied to corresponding region. These continua were defined using settings recommended in Volvo best practice.

The reference truck was placed in a wind-tunnel domain shaped as a cuboid with a height of 20 m, width of 36 m and length of 135 m. This arrangement will henceforth be referred to as the reference domain.

The air flow around the truck corresponded to a fluid continuum and was described by the region called Airstream. This region was limited by the surfaces of the truck and the walls of the domain. Three additional regions were defined: the radiator (RAD), the condenser (COND) and the charge air cooler (CAC). Each of these corresponds to a fluid continuum and these three together are called the cooling package. The boundary conditions, the solver settings, the settings of the surface mesh etc. were all set according to Volvo best practice.

The surfaces of the RAD, COND and CAC were assigned to both their own region and the Airstream region to limit the air flow. Interfaces were created between the regions which allowed air to pass through the surfaces into the other regions. The three parts of the cooling package were modeled as porous media with given coefficients for the pressure drop, which defined how much air flow could pass.

Volume meshes were needed to perform the CFD simulations. The volumes of the cooling package parts were sealed and volume meshes could be created inside these regions. The volume mesh of the Airstream leaked into the cab at a few places and let the air inside. In order to avoid this, the cab had to be sealed. This was an iterative process: generating mesh, checking the cab for leakage using the function leak detection, mend the leakage, generate new mesh and check again. The reparation was done on the surface geometry with a built-in function in STAR-CCM+.

The mesh type used was overall hexahedrals with prism layers close to the walls. The volume mesh of the reference domain is shown on a X-Z plane in Figure 7.1. All planes were defined in the *Derived Parts* folder.

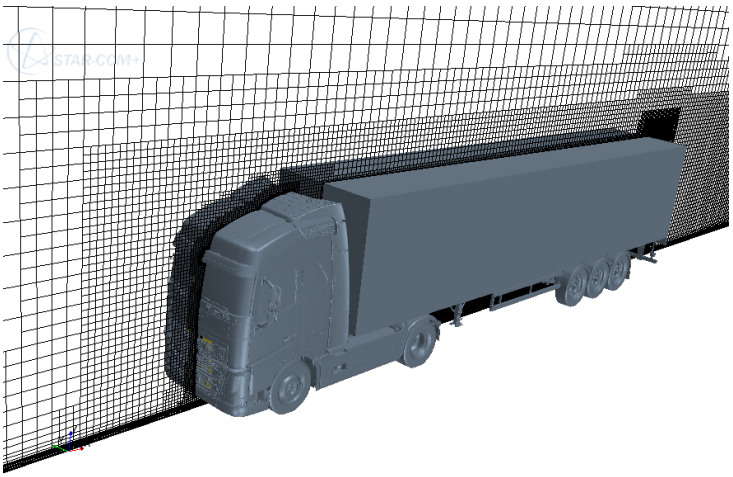

Figure 7.1: The volume mesh of the reference domain shown on the mid-plane in lateral direction.

The flow result obtained from the reference domain with all original parts of the reference truck will be called the reference case.

The reference case was obtained by using $U_\infty = 25$ m/s and solving for 4000 iterations. The inlet of the reference domain, located at a negative value of X, was set to a velocity inlet and the outlet was set to a pressure outlet. The flow was assumed to be fully turbulent in the whole domain and the turbulent intensity at the inflow was set to rather high. All remaining settings used to obtain the reference case are to be found in Volvo best practice and due to confidentiality they are not presented in this thesis.

The y^+ distribution of the reference case is illustrated in Figure 7.2.

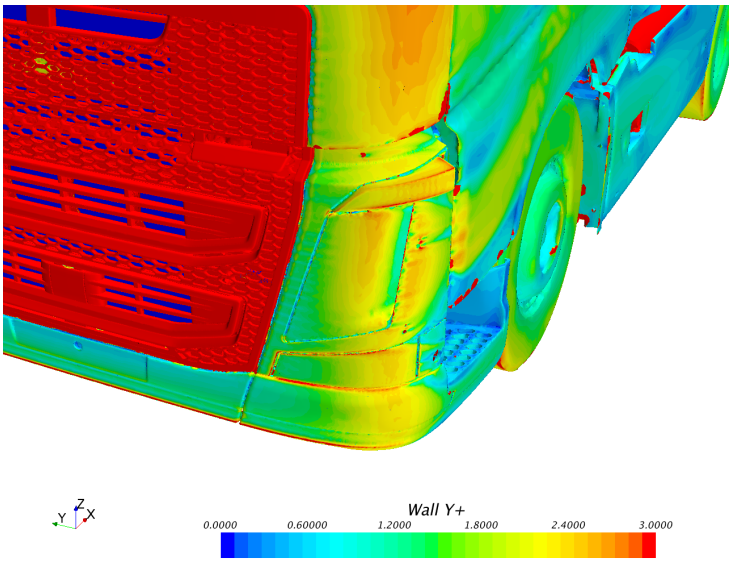

Figure 7.2: y^+ distribution of the reference case.

The aim of the Volvo best practice is to get a mesh close to y^+_{low}. The velocity field, C_D and the LSPG for the reference case are to be found in section 10.1.

8 Simplified Model

Simplifications were done both to the lower front and the domain. The simplification of the lower front was done in a manner such that one geometrical feature of the front corner could be changed without changing any other geometry, which is explained in this section.

8.1 Lower Front

A simplified lower front model was constructed to have similar shape as the original lower front. A sketch was created and determined from coordinates taken at the cross section located at Z=0.31 m of the original lower front. The sketch was extruded in both directions until its height corresponded to the original lower front height.

The front curvature was simplified to only consist of a straight line (1). The front corner was simplified to consist of a circular arc (2), with radius (r), and a following straight line (3), which created a positive draft angle (α) backwards, see Figure 8.1. The lines were tangential to the arc. The front corner radius will henceforth be referred to as r.

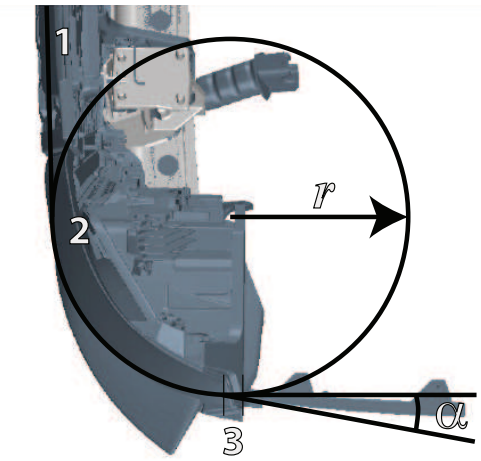

Figure 8.1: Top view of original lower front that illustrate the simplification. 1: Simplified front line, 2: Simplified front corner, 3: Simplified side line, r: Front corner radius, α: Draft angle.

The simplified lower front was created in a simplified environment. This environment consisted a small box with holes straight through and the CAC from the reference model. The holes through the small box can be seen in Appendix B. The flow through this box aimed to emulate the flow through the engine compartment in the reference domain. Even though only the CAC model was implemented in the simplified environment, the pressure drop applied corresponded to the complete cooling package. Since the CAC modeled the complete physics of the cooling package it will simply be referred to as the cooling package in this environment. The simplified environment along with the simplified lower front were placed in a small domain. This arrangement will henceforth be referred to as the simplified domain. The simplified domain is further described in section 8.2.

It is known that a sharp edge causes flow separation and therefore r was a given feature to investigate. In the beginning of the project, r was investigated using only $\alpha = 12°$ since it corresponded most to the original lower front, but very little flow separation was found in the simplified domain using $\alpha = 12°$, even for very small r. Hence, additional geometrical features needed to be considered since the purpose of this thesis was to investigate flow separation. It was found that $\alpha = 0°$ gave significant flow separation in the simplified domain and hence resulting in the most interesting cases. $\alpha = 0°$ and $\alpha = 12°$ are hereafter referred to as α_0 and α_{12} respectively.

The considered geometrical features are illustrated in Figure 8.2. Figure 8.2a shows the different r with α_0 and similarly Figure 8.2b shows different r with α_{12}. The approximated values of r and α most similar to the original lower front were estimated to 250 mm and 12° respectively. The distance between the end of the corner arc and the gap will be referred to as l_s.

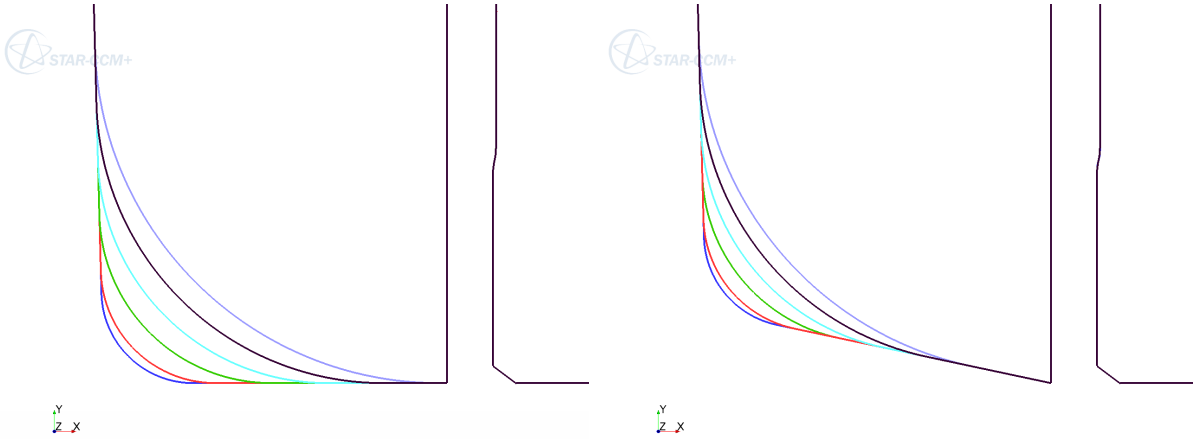

(a) Schematic illustration of different r with α_0.

(b) Schematic illustration of different r with α_{12}.

Figure 8.2: Schematic cross section of the simplified lower front.

There were other parameters considered when constructing the simplified lower front. The foremost point had to move forward a few mm from its original position in order to: vary r up to 300 mm, maintain a smooth shape during the adjustment and to have α between 0° and 12°.

It was desired to investigate the impact of the geometrical features with the same prerequisites of the flow as in the reference case. To compare and secure these prerequisites, mainly three parameters were used. These parameters are the flow around the corner, mass flow through the cooling package and the flow through the gap. These parameters are strongly connected to the mass flow through the front. Therefore, a lot of effort was put in adjusting the holes in the front to obtain as similar mass flow as possible through it compared to the reference case. The pattern and the size of the holes in the front were designed during an iterative process, where the three flow parameters from the simplified domain were compared with the same parameters from the reference case. The comparison was done using the simplified lower front with $r = 250$ mm and α_{12}.

The original front corner is very complex, for example, containing side turn indicator and bumper that bugles out.

To compare the maximum velocity around the corner a height between the bumper and side turn indicator was chosen. The chosen height was located at Z=0.31 m, where the corner radius was fairly constant.

If, for example, the mass flow through the cooling package differed in a significant matter, a change in hole sizes or a change in quantity of holes was required. Table 8.1 shows the comparison between the final flow obtained in the simplified domain and the reference case. The resulting dimensions of the holes can be found in Appendix B.

Table 8.1: Comparison of the final flow in the simplified domain and the reference case.

	Reference	Simplified	Difference [%]
Cool. package: mass flow [kg/s]	3.01	3.19	5.98
Front corner: max vel. [m/s]	39	42	7.69
Gap: average vel. [m/s]	10	14	40

The final simplified lower front can be seen in Figure 8.3.

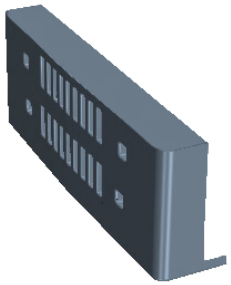

Figure 8.3: Final simplified lower front.

A few simulations were carried out in the reference domain with replaced lower front. A comparison of the original lower front and the simplified lower front placed in the reference domain can be seen in Figure 8.4.

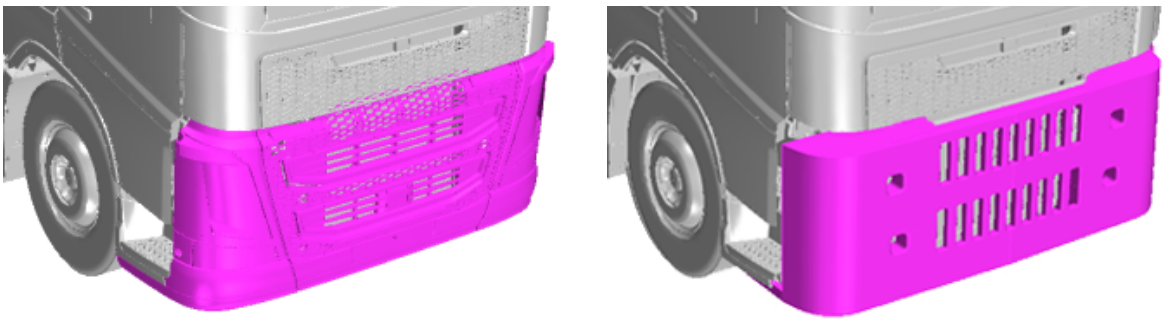

(a) Original lower front. **(b)** Simplified lower front.

Figure 8.4: Comparison of original lower front and simplified lower front placed in the reference domain.

8.2 Domain

A simulation in the reference domain takes a lot of time and in this investigation a huge amount of simulations had to be done for different values of the geometrical features. All theses simulations were not possible to perform using the reference domain within a reasonable time limit since it consisted of about 92 million cells. To save time, while tuning parameters and investigating the effects of the geometrical features, a simplified domain was used which consisted of about 34 million cells.

The simplified domain focused on the front corner and the adjacent flow. In this domain there is a small gap between the simplified lower front and the small box to emulate the flow in the reference domain, where there is a gap between the door and the lower front. The simplified domain is shown in Figure 8.5.

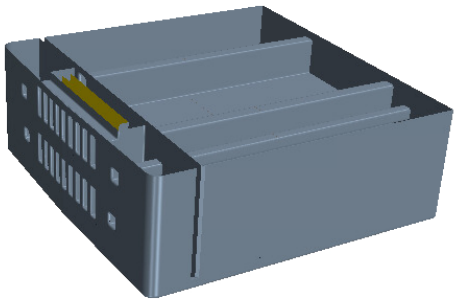

Figure 8.5: Simplified domain.

The small domain was shaped as a cuboid and its dimensions are stated in Table A.3. The top of the domain was flush with the simplified lower front and the small box. The boundary conditions of the top and the sides of the domain were set to symmetry planes. The boundary condition of the front side was set to a velocity inlet, the boundary condition of the back side was set to a pressure outlet and the boundary condition of the bottom was set to a wall. The flow in the simplified domain was assumed to be fully turbulent and the applied turbulent intensity of the inflow and the outflow are specified in Table A.5 in Appendix A.

According to theory in section 4.3, flow separation on a cylinder occurs in a laminar matter for $\mathrm{Re}_d < 2 \times 10^5$. Applying $U = U_\infty = 25$ m/s, $\mu = 1.85 \times 10^{-5}$ kg/ms and $L = d = 2r$ to eq 3.3, Re_d was calculated for $r = 80$ mm (the smallest r used). This gave $\mathrm{Re}_d \approx 216\ 216$, which is larger than 2×10^5 and hence the assumption of fully turbulent flow was considered reasonable.

8.3 Mesh Generation

The mesh settings of the parts in the simplified domain can be found in Appendix A. Figure 8.6 shows the volume mesh of the simplified domain on the mid-plane in lateral direction.

The mesh type used in the simplified domain is consistent with the reference domain, which consisted of overall hexahedrals with prism layers close to the walls.

Figure 8.7 shows the mesh around the left hand side (LHS) front corner on a X-Y plane. The front corner is hidden in this figure.

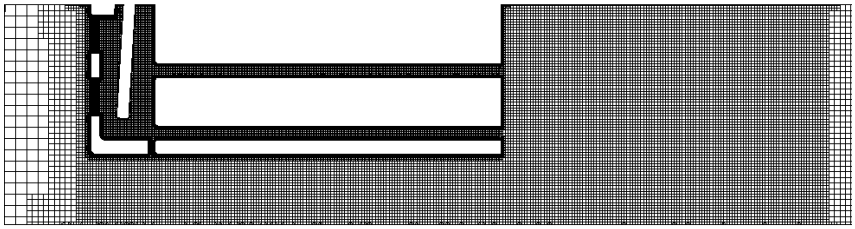

Figure 8.6: Volume mesh of the simplified domain shown on the mid-plane in lateral direction.

In this study, it was desirable to investigate meshes of both y^+_{low} and y^+_{high}. The total prism layer height was 16 mm. For y^+_{low} the amount of prism layers was 30 and the first prism layer height was 0.01 mm. A higher value of y^+ at the corner was obtained by moving the first prism layer away from the wall. This was done using less prism layers and keeping the total prism layer height as well as the prism layer stretching constant. The mesh with y^+_{high} ended up with 10 prism layers and a first prism layer height of 1.14 mm.

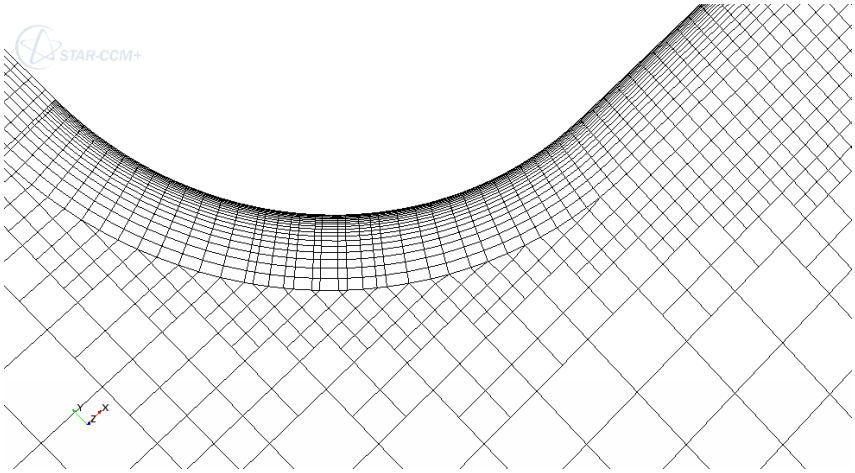

Figure 8.7: Top view. Mesh around the LHS front corner.

8.4 y^+ Distribution

It is desirable to use as few cells as possible by using wall functions. This requires y^+_{high}, which spare computational power and time. An investigation of the effects of using y^+_{high} in comparison to solving the entire boundary layer, i.e y^+_{low}, were made by comparing C_D. In Figure 8.8b, C_D is nearly 200 drag counts higher using y^+_{high}. This is a significant difference and thus y^+_{high} does not correspond very well to y^+_{low}.

It was found that the lower edge (bumper) was the main reason to the high C_D value since this edge was sharp, which caused a flow separation. As can be seen in Figure 8.8b, the velocity magnitude around this edge differs from the the velocity magnitude in Figure 8.8a.

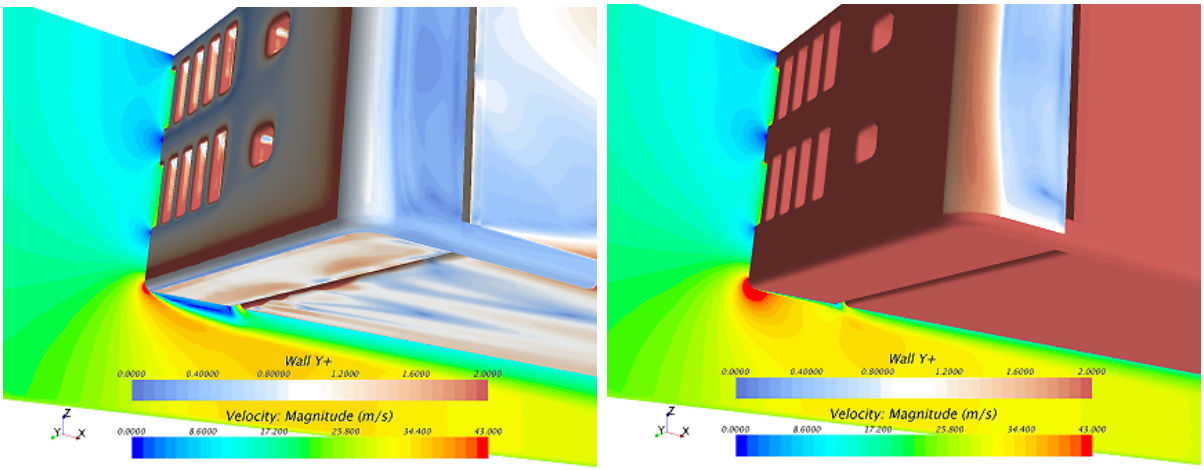

(a) Visualization of y^+_{low}. $C_D \approx 0.815$.

(b) Visualization of y^+_{high}. $C_D \approx 0.624$.

Figure 8.8: Simplified domain. Comparison of the velocity magnitudes for y^+_{low} and y^+_{high}.

This flow separation was not desired since the purpose was to investigate the effects of the front corners. Thus, there were two options: either increase the radius of the bumper or solve with y^+_{high}. Since the original lower front has a sharp edge in this region it was decided to keep the sharp edge. When comparing y^+, changes were only made to the front corner region. The rest were always set to $y^+ \approx 30 - 100$ to avoid this flow separation. $y^+_{low,c}$ will be used to denote y^+_{low} around the front corners and y^+_{high} around the other parts.

9 Post processing

A short review of the post processing done to obtain the results is given in this section.

9.1 Local Streamwise Pressure Gradient

The pressure gradient was not a predefined function in STAR-CCM+. Therefore, the LSPG was calculated from the dot product between vectors of pressure difference and normalized velocity vectors, according to eq 4.6. Since the real instantaneous velocity field was not available, the velocity field obtained by using k–ε model with realizable coefficient was used instead. This was done creating a custom function in the *Function* folder, which resides in the *Tool* folder.

The LSPG values just around the front corner were displayed on the front corner surface and to visualize the behavior of the flow and facilitate identification of flow separation the streamlines were projected on the front corner surface as well.

9.2 Accumulated Drag Coefficient

By calculating accumulated C_D a longitudinal relation was obtained. This made it possible to identify how much each part contributed to the total C_D. This was done by running a macro developed by CD-adapco where C_D is calculated and accumulated throughout the longitudinal direction.

9.3 Plane

Planes were specified in the *Derived Parts* folder. The most used ones are a X-Y plane at Z=0.31 m (ground is located at $Z = -0.69$ m) and a X-Z plane at Y=0.0 m. These were used to visualize velocity magnitude and velocity directions, e.g. in Figure 8.8.

10 Results

The results obtained from both the reference domain and the simplified domain are presented in this section. The results are divided into C_D as a function of r, velocity field and LSPG. In addition, results of different y^+ distributions are compared. The most important result is the variation of C_D for the different sets of the geometrical features.

10.1 Reference Case

The simulation was performed using the recommended settings in Volvo best practice.

10.1.1 Drag Coefficient

The result of C_D was obtained to 0.475 for the reference case.

The accumulated C_D was plotted against the longitudinal position of the truck in Figure 10.1.

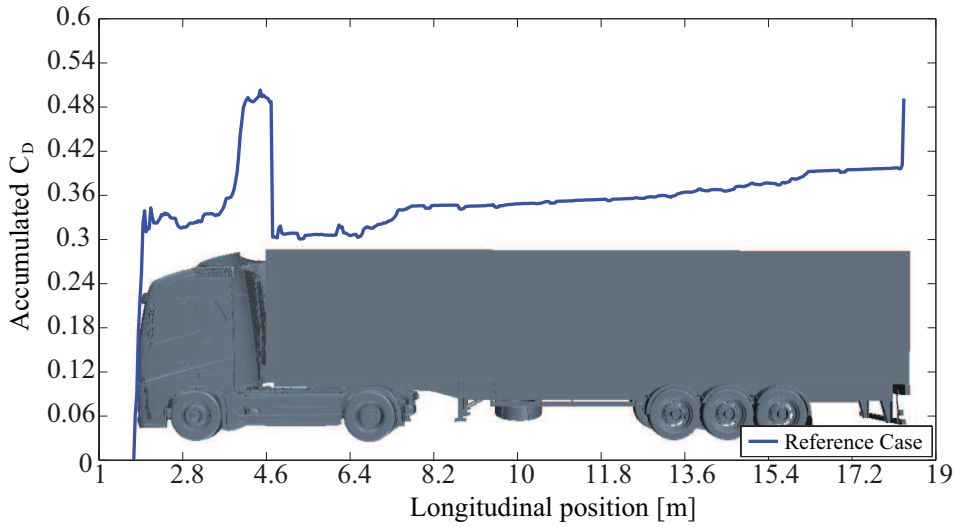

Figure 10.1: Reference case. Accumulated C_D in regard to longitudinal position.

The foremost point of the front of the truck is located at a longitudinal position of 1.81 m. As can be seen from Figure 10.1, the front gives the largest contribution to C_D. This is seen by the large increase of the accumulated C_D. The second largest contributor is the rear of the semi-trailer. Further, it can be seen that the large peak of the accumulated C_D at the rear of the cab is regained at the front of the semi-trailer, which is due to the low pressure in this region. It is even low enough to give a negative contribution to C_D. The impact on the drag due to the rear and the gap behind the cab has been investigated further in other works. In this thesis, focus is on the corners of the lower front, located at a longitudinal position of approximately 1.83 m.

10.1.2 Velocity Field

Figure 10.2 shows the velocity magnitude and direction for the reference case. These are shown on the X-Y plane defined in section 9.3.

The velocity magnitude reaches its maximum value around 35 m/s at the corner, as expected. Note that a massive flow separation can be seen first behind the gap.

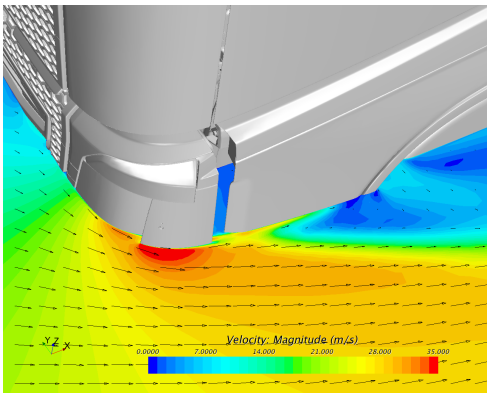

Figure 10.2: Reference case. Velocity magnitude and direction on the X-Y plane at Z= 0.31 m.

To further illustrate the flow separation for the reference case, an iso surface for $p_{tot} = 0$ is shown in Figure 10.3.

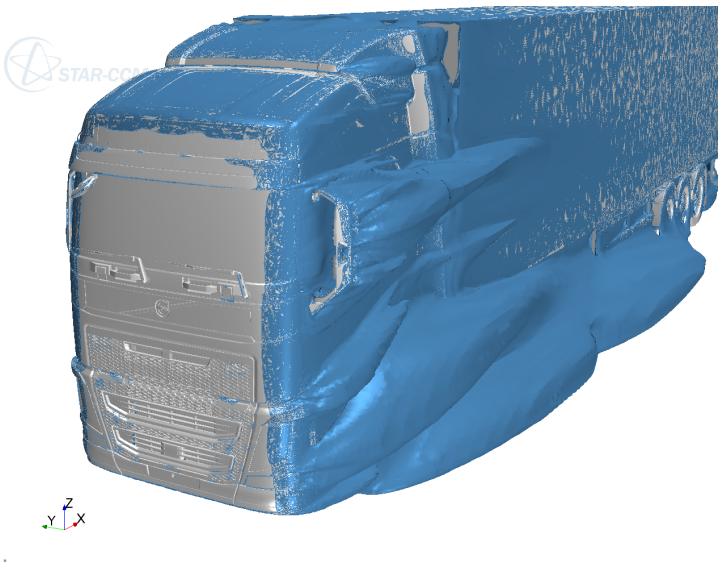

Figure 10.3: Reference case. Iso surface for $p_{tot} = 0$.

Large wake structures appear around the truck, which indicates energy losses in the flow, mainly due to separated regions and turbulence. Separation points are indicated as deviations from the original surface of the truck, thus separation occurs even before the gap at certain heights of the lower front corner. Compare this with Figure 10.2, where separation does not occur before the gap at that specific height.

10.1.3 Local Streamwise Pressure Gradient

The LSPG was calculated for the reference case and the result is shown in Figure 10.4.

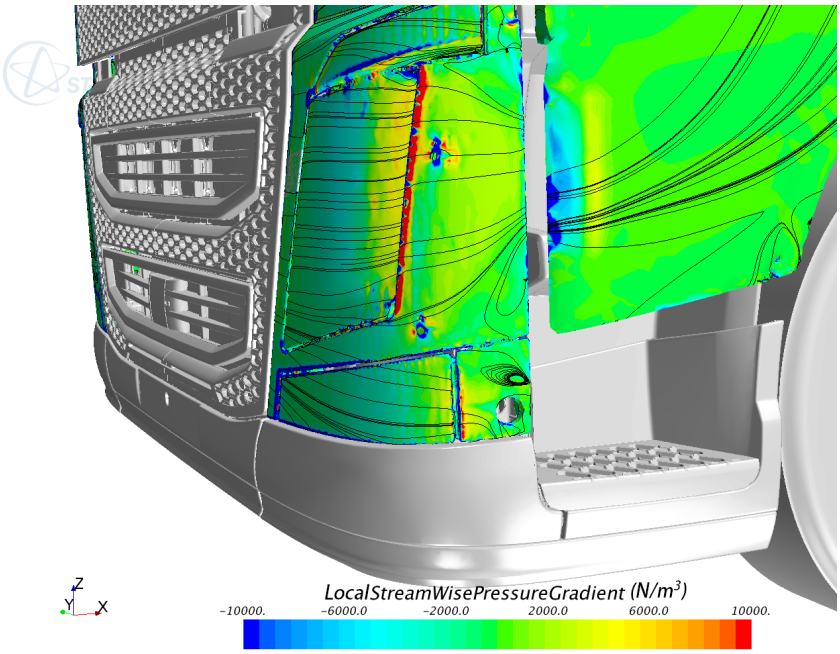

Figure 10.4: Reference case. LSPG around the lower LHS front corner.

Note that the LSPG has a negative value close to zero and decreases at the beginning of the lens. Then as traveling pass the lens the LSPG gradually increases ended up with a quite high positive one in the end of the lens, see the bright yellow area just before the tip of the headlamp panel in Figure 10.4. Between the end of the lens and the tip of the headlamp panel a discontinuous jump to the highest value occurs, which is caused by the sharp edge. The highest value of the LSPG is around 10^4 N/m^3. After the tip of the headlamp panel a sudden change to a much lower positive value occurs, which remains until the gap. After the gap an area of a strong negative value of the LSPG is found, otherwise after the gap the LSPG remains positive.

10.2 Geometrical Features

The following results are from the simplified domain, i.e. the simplified front and environment simulated in the small domain. In the simulations two different geometrical features were investigated, r and α. All results were simulated using both $y^+_{low,c}$ and y^+_{high}. The mesh settings, boundary conditions and physical models used in the simplified domain can be found in Appendix A.

10.2.1 Drag Coefficient

Figure 10.5 shows how C_D changes for varying r for different sets of α and y^+. Comparisons of α_0 and α_{12}, using both y^+_{high} and $y^+_{low,c}$ are found in the figure.

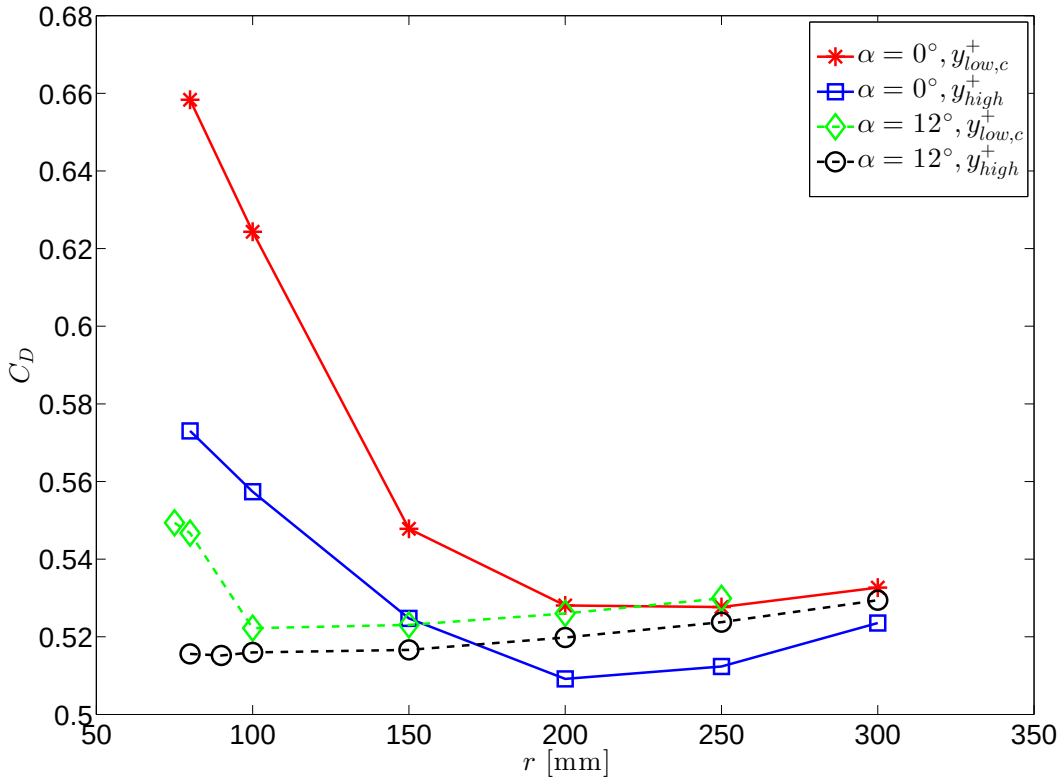

Figure 10.5: Simplified domain. C_D as a function of r for α_0 and α_{12}, using both y^+_{high} and $y^+_{low,c}$.

From the curves in Figure 10.5 it can be seen that the minimum C_D for α_0 occurs around $r = 200$ mm for both y^+_{high} and $y^+_{low,c}$. C_D decreases for increasing r between 80 mm and 200 mm, since less and less flow separation occurs. For increasing r between 200 mm and 300 mm C_D slightly increases again. For $r \geq 200$ mm there is no significant flow separation at the corner and C_D increases with increasing r due to shorter l_s.

For both α_0 and α_{12}, C_D is overall lower for y^+_{high} in regards to $y^+_{low,c}$. The difference between y^+_{high} and $y^+_{low,c}$ is significant for smaller r and the difference decreases as r increases. For the curves of α_0, the significant difference remains until $r = 150$ mm and corresponding point for the curves of α_{12} is found at $r = 100$ mm.

The curve corresponding to α_{12} and $y^+_{low,c}$ has its minimum C_D around $r = 100$ mm, while the curve corresponding to α_{12} and y^+_{high} has its minimum below $r = 100$ mm.

The trend of the curve for α_{12} and y^+_{high} shows an increased C_D with increasing r. The shape of this curve differs from the others since C_D remains low even for very small r. This is since no flow separation was found for the considered range of r and therefore C_D is only increased with increasing r due to shorter l_s.

When there is no significant flow separation at the corner $\alpha > 0°$ is expected to have a higher C_D compared to $\alpha = 0°$. For $y^+_{low,c}$ this effect is seen in Figure 10.5, where α_0 and α_{12} intersects for r between 200 mm and 250 mm. For $r = 250$ mm the C_D value of α_{12} is the higher one. The same effect can be seen for y^+_{high} around $r = 150$ mm.

10.2.2 Velocity Field

The results of the simulations for the simplified domain regarding the velocity field are found in Figure 10.6, Figure 10.7b and Figure 10.8.

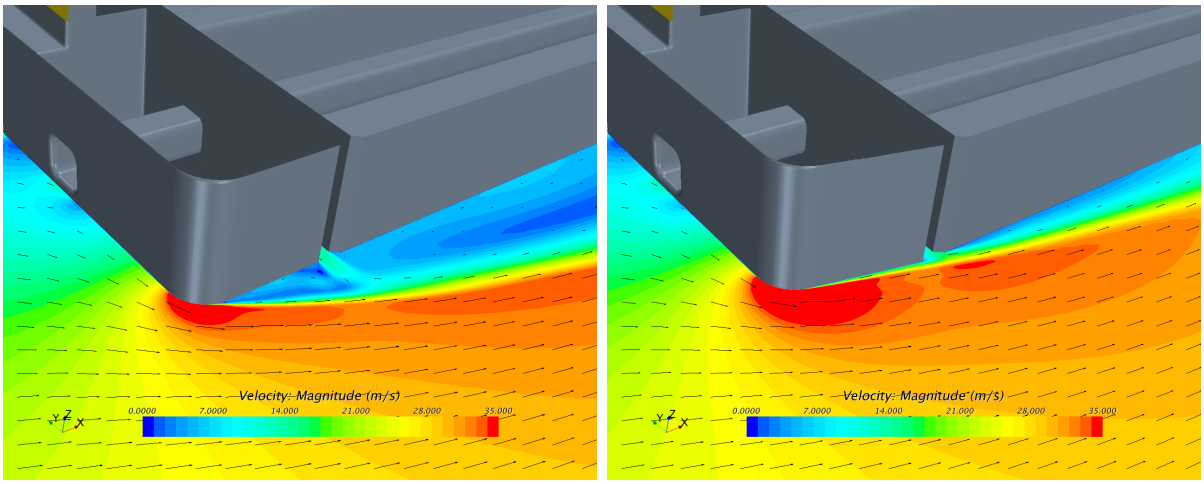

(a) α_0. **(b)** α_{12}.

Figure 10.6: Simplified domain. Velocity magnitude and direction on the X-Y plane at Z= 0.31 m for $r = 80$ mm and $y^+_{low,c}$.

Figure 10.6 compares α_{12} and α_0 for $r = 80$ mm. Flow separation occurs in both cases. Right in front the body the velocity is zero but the flow accelerate around the corner and the highest velocity is reached at the corner crest, above 35 m/s. In the point of separation the flow breaks off from the surface and a separation bubble is created behind. Note the massive flow separation for α_0 compared to α_{12}. For the case of α_{12} there is also a larger area of high velocity around the corner.

Figure 10.7b shows the impact on the flow caused by a shorter l_s.

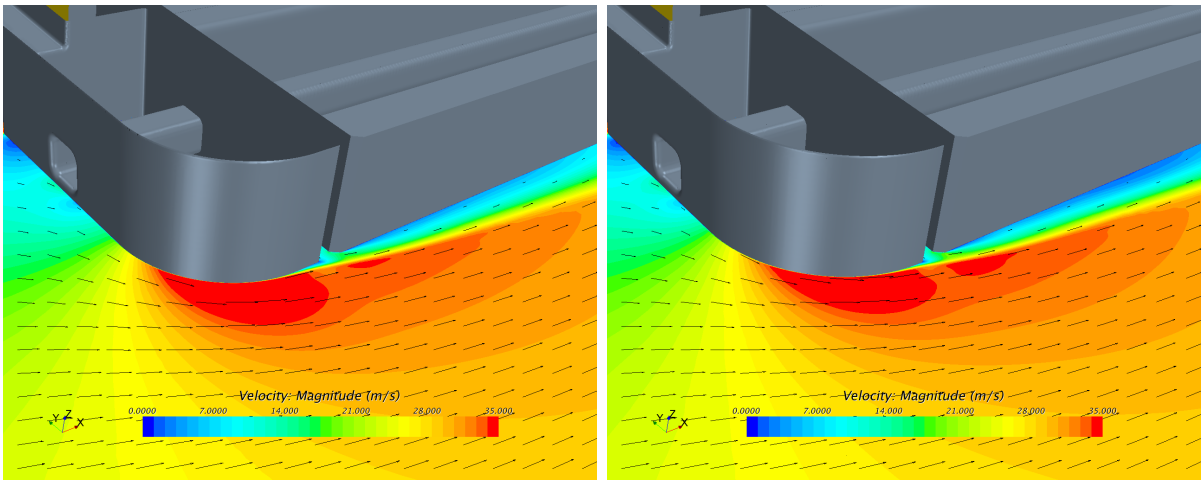

(a) $r = 250$ mm. **(b)** $r = 300$ mm.

Figure 10.7: Simplified domain. Velocity magnitude and direction on the X-Y plane at Z= 0.31 m for α_0 and $y^+_{low,c}$.

Note the difference of the separation bubbles behind the gap. There are lower velocities close to the wall for the larger r, i.e. shorter l_s. This applies to all cases when there is no flow separation at the corner. For a shorter l_s the flow around the corner has less space to straighten up before the gap, which gives a higher mass flow out of the gap. Since there is more flow out of the gap and less longitudinal flow close to the wall before the gap, less flow is pulled along the wall. This causes lower velocities close to the wall in the separation bubble. Figure 10.8 shows that the impact of shorter l_s is the same for α_{12}.

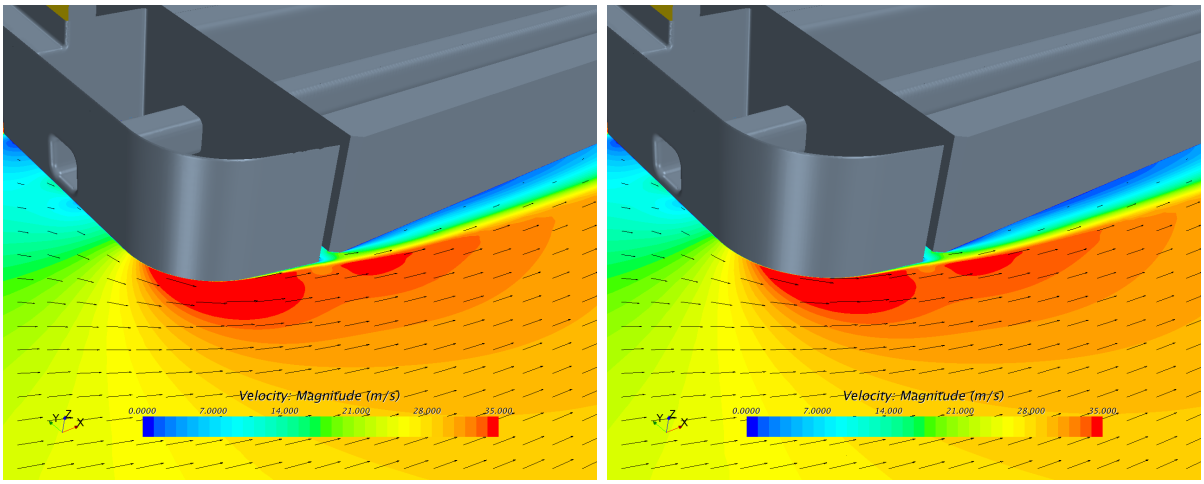

(a) $r = 200$ mm. **(b)** $r = 250$ mm.

Figure 10.8: Small domain. Velocity magnitude and direction on the X-Y plane at Z= 0.31 m for α_{12} and $y^+_{low,c}$.

Compare Figure 10.8b and Figure 10.7a. In these cases there are no significant flow separation before the gap. From the figures it can be seen that there are differences in the flows behind the corner crest close to the wall. The angled geometry for α_{12} causes the streamlines to deviate from the longitudinal direction when reaching the gap. Hence, a higher mass flow out of the gap is present compared to α_0. Since there is less flow in longitudinal direction close to the wall before the gap and a higher mass flow out of the gap, less flow is pulled along the wall. This in turn leads to lower velocities close to the wall behind the gap for the cases with α_{12} compared to the cases with α_0.

10.2.3 Local Streamwise Pressure Gradient

The LSPG for the configurations of α_0 and r varying between 80 mm and 300 mm are illustrated in Figure 10.9 and Figure 10.10.

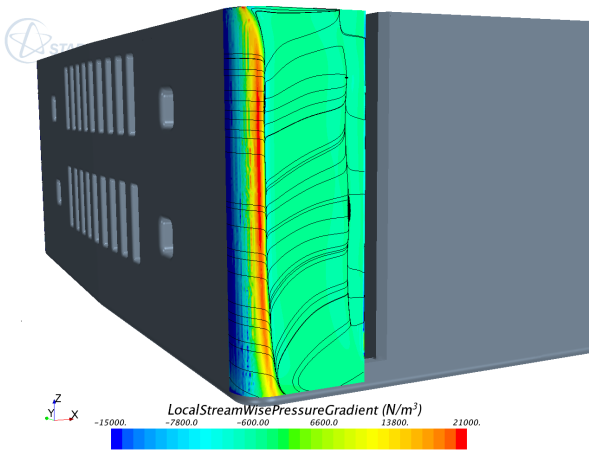

(a) $r = 80$ mm and $y^+_{low,c}$.

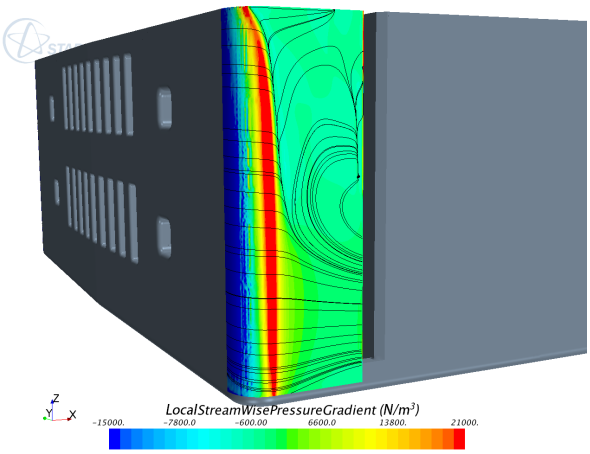

(b) $r = 80$ mm and y^+_{high}.

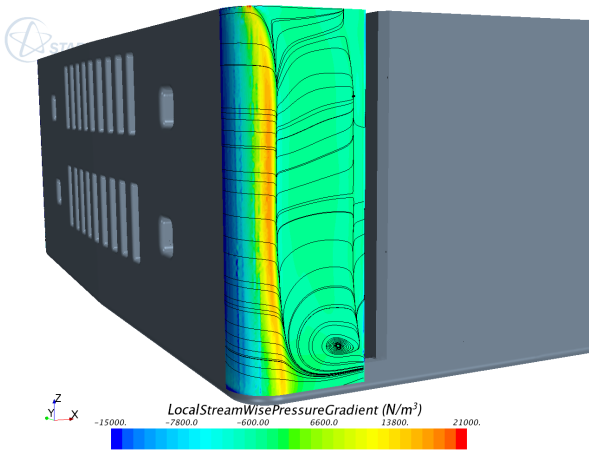

(c) $r = 100$ mm and $y^+_{low,c}$.

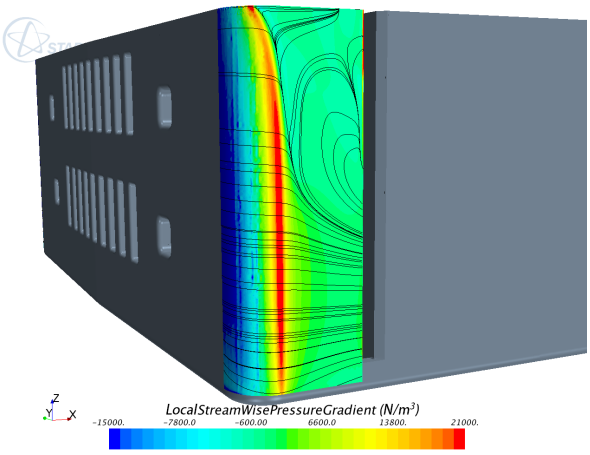

(d) $r = 100$ mm and y^+_{high}.

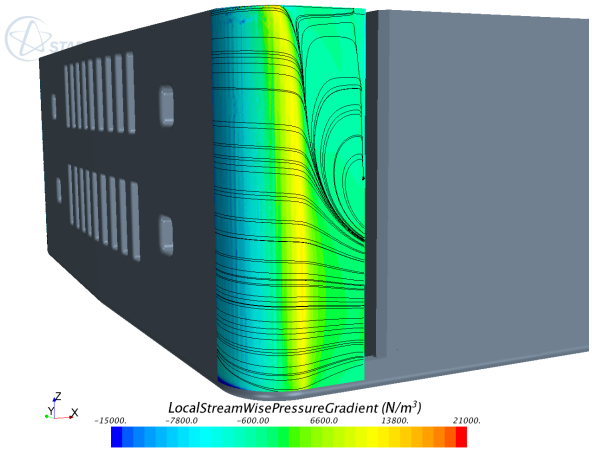

(e) $r = 150$ mm and $y^+_{low,c}$.

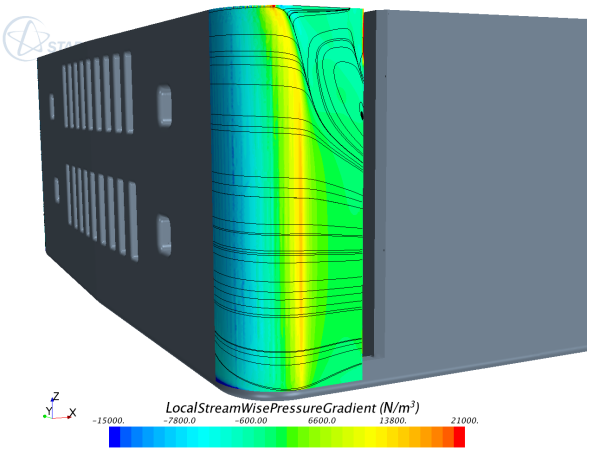

(f) $r = 150$ mm and y^+_{high}.

Figure 10.9: Simplified domain. LSPG for r between 80 mm and 150 mm with α_0. The left column shows $y^+_{low,c}$ and the right column shows y^+_{high}.

Just at the beginning of the corner in Figure 10.9a the LSPG is strongly negative, around -1.5×10^4 N/m^3, thereafter it gradually increases and changes sign around the corner crest. The LSPG continues to growth rapidly reaching its maximum value, approximately 2.1×10^4 N/m^3, some distance after the crest of the corner. After the maximum value the LSPG decreases rapidly and for a value of around 3×10^3 N/m^3, flow separation occurs. Just after the flow separation the LSPG is negative but increases to a slightly positive value, which overall remains until the gap. The exceptions are some regions where slightly negative LSPG occur.

There are some deviations in the behavior of the LSPG described above. In the upper region the LSPG reaches the strong positive value slightly before the middle region does. This is likely due to the symmetry boundary condition. Also in the lower region the strong value occurs at some distance later.

The same pattern as in Figure 10.9a can be seen in Figure 10.9b, but it has a wider spread of the extreme values, i.e. a larger region has a value lower or equal to -1.5×10^4 N/m^3 and a larger region has a value larger or equal to 2.1×10^4 N/m^3. Note also that the maximum value occurs later than for $y^+_{low,c}$, the transition from around -1.5×10^4 N/m^3 to 0 N/m^3 is faster and transition from 0 N/m^3 to maximum is slower. The flow separation occurs throughout the entire height for $y^+_{low,c}$ but only in the upper region for y^+_{high}.

For $r = 100$ mm the pattern is generally the same as for $r = 80$ mm, but the maximum value is lower. The highest LSPG is around 1.8×10^4 N/m^3 for $y^+_{low,c}$ and around 2.1×10^4 N/m^3 for y^+_{high}. Note that the streamlines follow the surface of the lowest part in Figure 10.9c, hence no flow separation occurs there.

As r increases the maximum value is lower, occurs later and the transitions are smoother for both $y^+_{low,c}$ and y^+_{high}. Additionally, as r increases the flow separation is more restricted to the upper region.

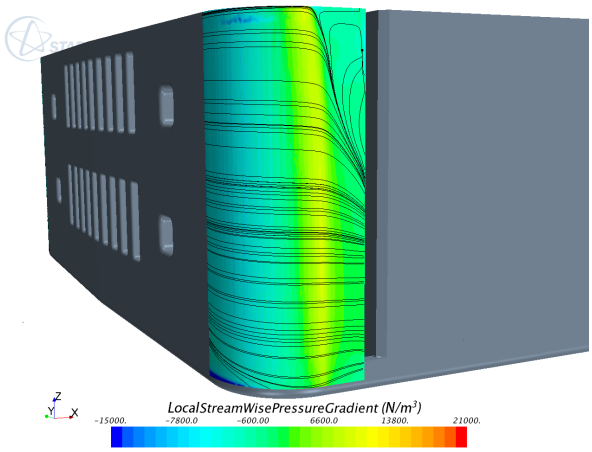

(a) $r = 200$ mm and $y^+_{low,c}$.

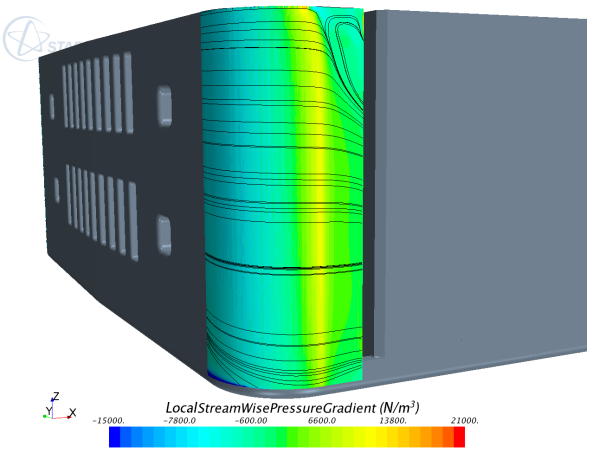

(b) $r = 200$ mm and y^+_{high}.

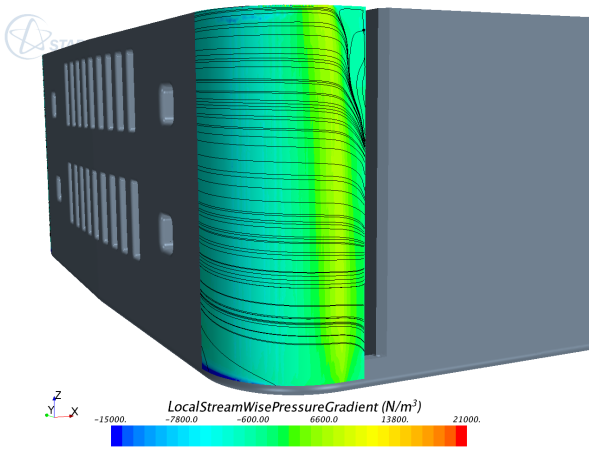

(c) $r = 250$ mm and $y^+_{low,c}$.

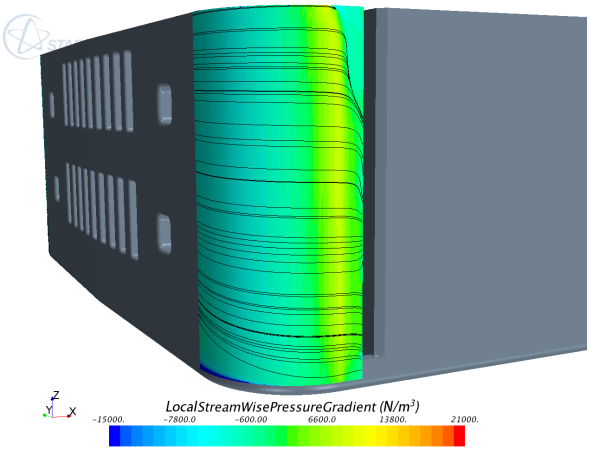

(d) $r = 250$ mm and y^+_{high}.

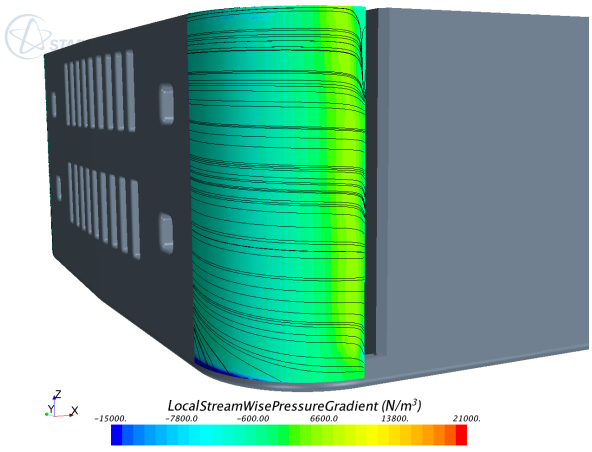

(e) $r = 300$ mm and $y^+_{low,c}$.

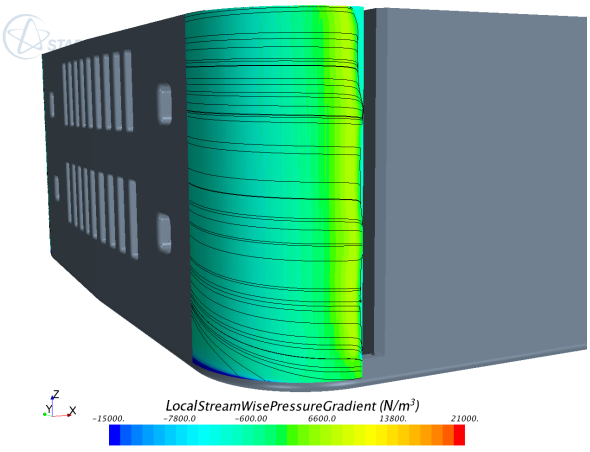

(f) $r = 300$ mm and y^+_{high}.

Figure 10.10: Simplified domain. LSPG for r between 200 mm and 300 mm with α_0. The left column shows $y^+_{low,c}$ and the right column shows y^+_{high}.

As r is further increased the flow separation is more and more restricted to the upper region. When r reaches 300 mm there is almost no flow separation, see Figure 10.10. The differences between $y^+_{low,c}$ and y^+_{high} are less noticeable as r increases.

Figure 10.11 shows the LSPG for the cases with α_{12} and r between 80 mm and 150 mm.

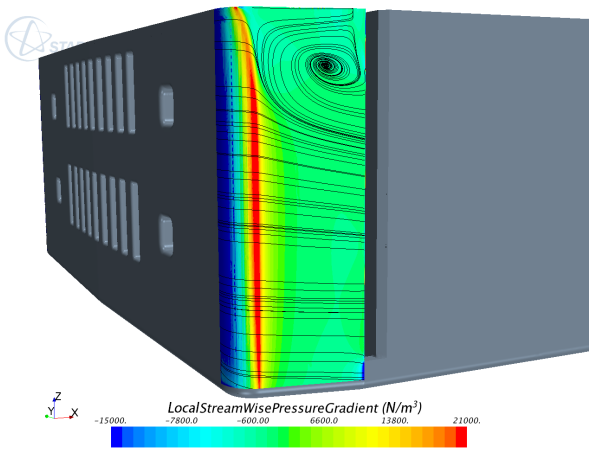

(a) $r = 80$ mm and $y^+_{low,c}$.

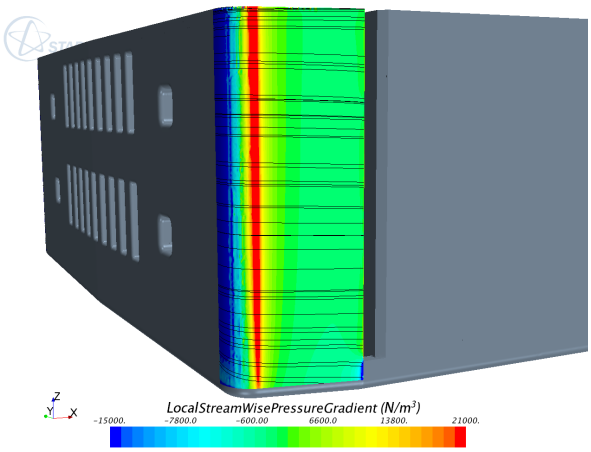

(b) $r = 80$ mm and y^+_{high}.

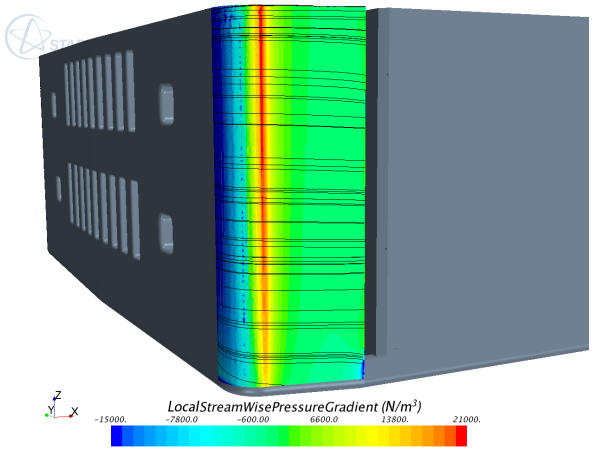

(c) $r = 100$ mm and $y^+_{low,c}$.

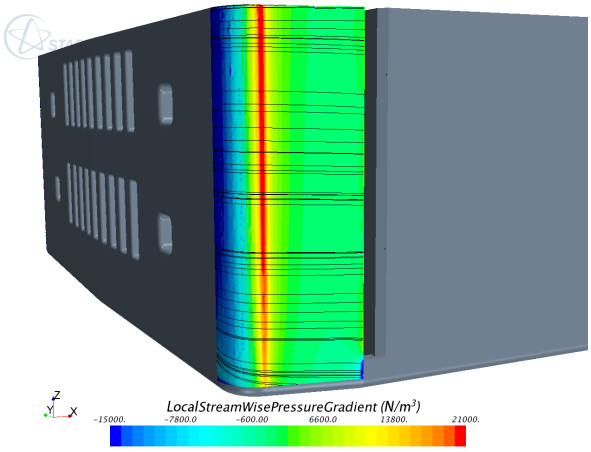

(d) $r = 100$ mm and y^+_{high}.

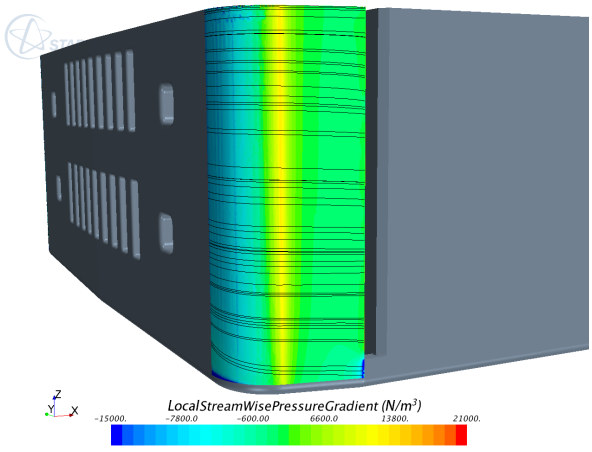

(e) $r = 150$ mm and $y^+_{low,c}$.

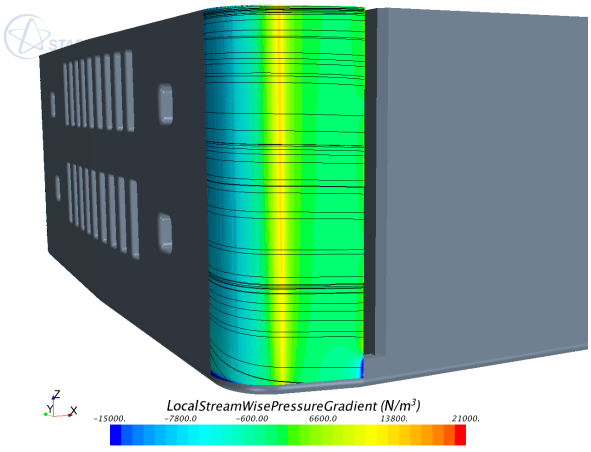

(f) $r = 150$ mm and y^+_{high}.

Figure 10.11: Simplified domain. LSPG for r between 80 mm and 150 mm with α_{12}. The left column shows $y^+_{low,c}$ and the right column shows y^+_{high}.

The case with $y^+_{low,c}$ and $r = 80$ mm is the only case with α_{12} where the simulation clearly predicts a flow separation, see Figure 10.11a. As for α_0 the high extreme value of LSPG are more spread out for y^+_{high}, i.e. a larger region has a LSPG above $2.1{\times}10^4$ N/m^3.

It is clear that the difference between varying r is much less with α_{12} compared to α_0, compare Figure 10.9 and Figure 10.11.

The LSPG for r larger than 150 mm and α_{12} do not add anything new to the pattern and hence they are not presented.

From the results in this section it is concluded that flow separation is not connected to a specific maximum value of LSPG but it seems that it is connected to the positive second derivate of the local streamwise pressure.

10.3 Comparison of Different y^+ Distributions

The impact of different mesh densities was investigated by varying y^+ between 1–100. This investigation was performed using the simplified domain.

The distribution of four different y^+ for $r = 80$ mm are shown in Figure 10.12.

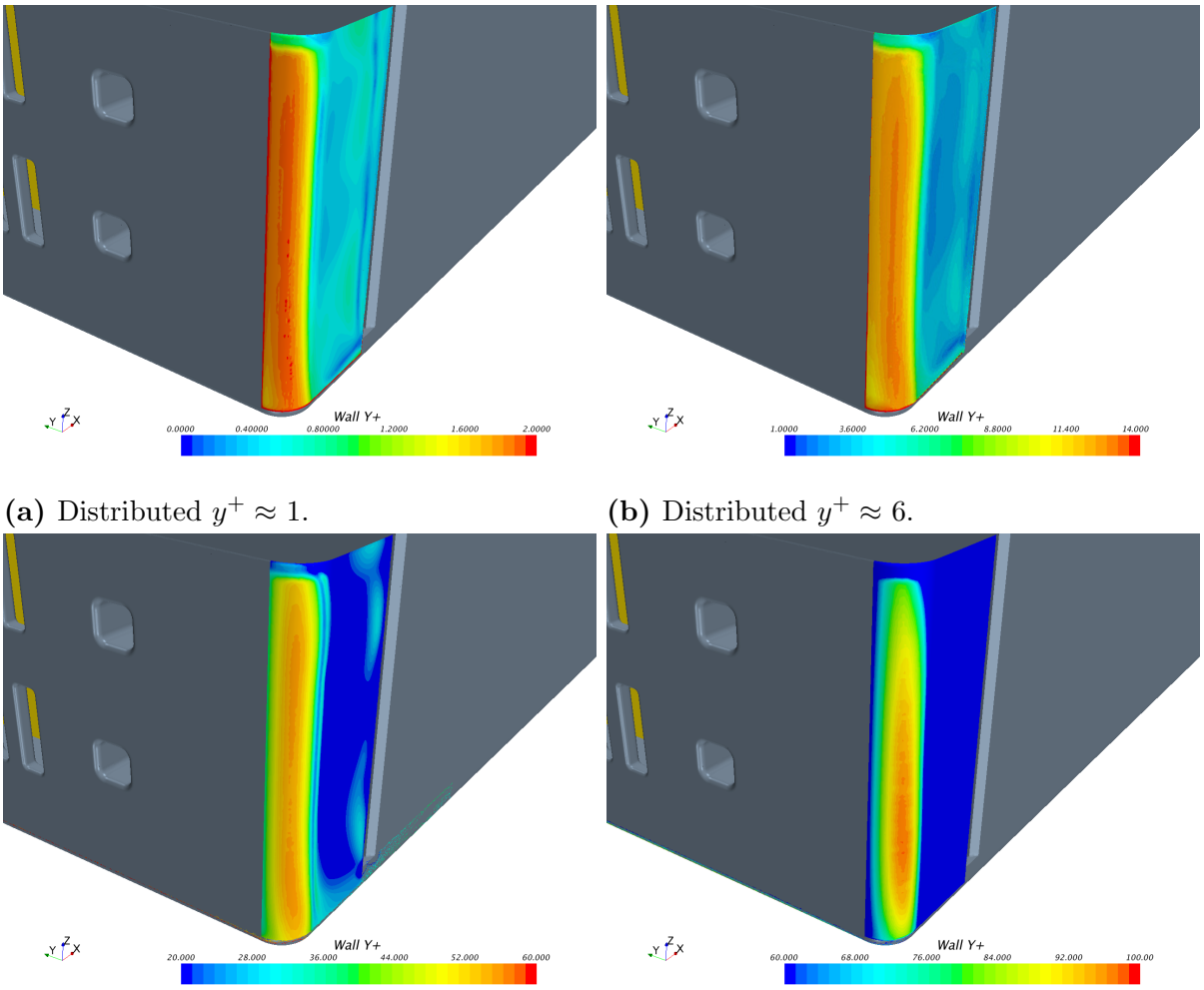

(a) Distributed $y^+ \approx 1$.

(b) Distributed $y^+ \approx 6$.

(c) Distributed $y^+ \approx 30$.

(d) Distributed $y^+ \approx 60$.

Figure 10.12: Simplified domain. Distributed y^+ for $r = 80$ mm.

Note that the same colours correspond to different values of y^+ in the different images in Figure 10.12. For example, Figure 10.12a shows a distribution where y^+ varies between 0–2.8 but Figure 10.12d shows a distribution where y^+ is overall higher and its maximum value is 100. The reason for the different distributions for the same r is that for constant values of y and ν, y^+ is only dependent on the velocity parallel to the surface. A larger value of this velocity gives a higher τ_w, which in turn gives a larger u^* and therefore a higher y^+, see eq. 5.1.

For the case of $r = 80$ mm and α_0, separation occurs a bit after the corner crest and a separation bubble is created behind this point, see Figure 10.7a, where the velocities are low which explains the region of low y^+ in Figure 10.12.

The investigation was done for some values between $y^+ \approx 1$ and $y^+ \approx 60$. The results are shown in Figure 10.13. The values of y^+ labeled in Figure 10.13 are the average values of the different y^+ distributions of the entire colored surface, from the beginning of the corner arc to the gap, see Figure 10.12.

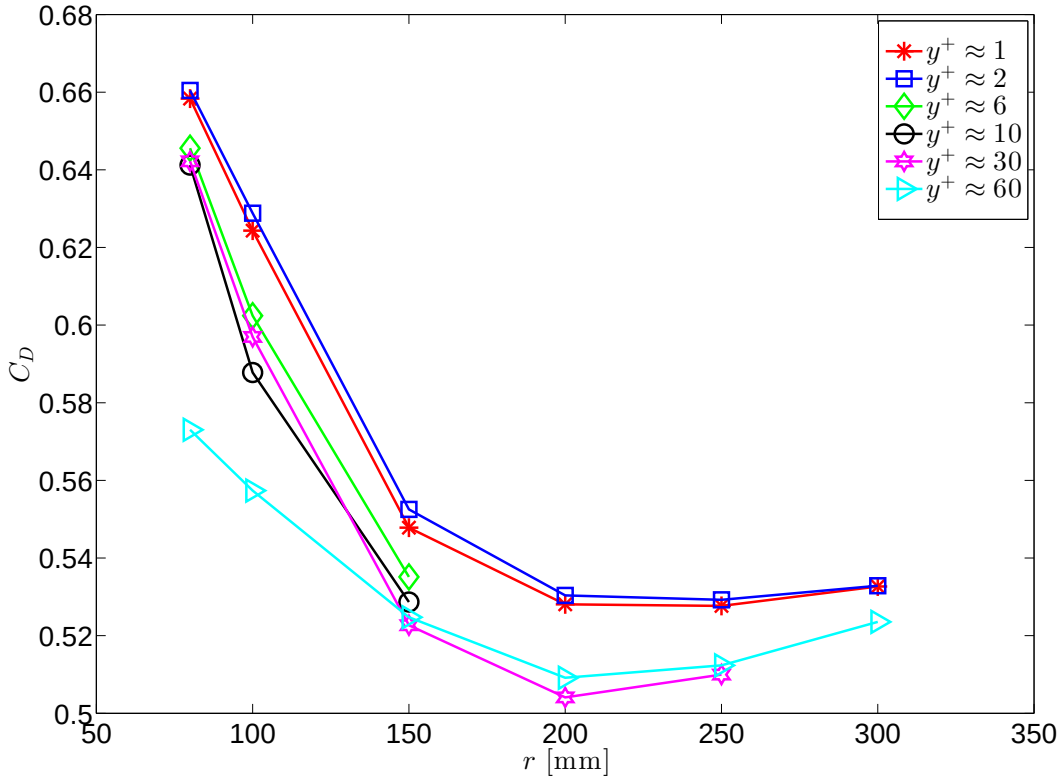

Figure 10.13: Simplified domain. C_D as a function of r for α_0 and varying averaged y^+.

The highest C_D curve is obtained with the averaged $y^+ \approx 2$, see Figure 10.13. This curve is very similar to the curve with the averaged $y^+ \approx 1$. For small r the curve for averaged $y^+ \approx 60$ deviates significant from the other curves. From these results it is seen that the separation is delayed by poor resolution which gives a lower C_D. The difference in C_D between $y^+ \approx 1 - 2$ and $y^+ \approx 6 - 30$ is nearly constant for $r \leq 150$ mm.

10.4 Comparisons in the Reference Domain

The original lower front and the simplified lower front were compared in the reference domain (the reference tuck in the wind-tunnel domain). A comparison of the different configurations is shown in Figure 8.4. Some results of the reference case (original lower front in reference domain) have already been presented in section 10.1. The flow results obtained from the reference domain with the simplified lower front and different sets of the geometrical features are referred to as the simplified cases.

10.4.1 Drag Coefficient

The C_D values of the simplified cases, for both α_0 and α_{12}, were compared with the C_D value of the reference case. Figure 10.14 shows C_D as a function of r. The values of r and α of the original lower front have been approximated to 250 mm and 12°. It can be seen that both α_0 and α_{12} with $r = 250$ mm have lower C_D than the reference case.

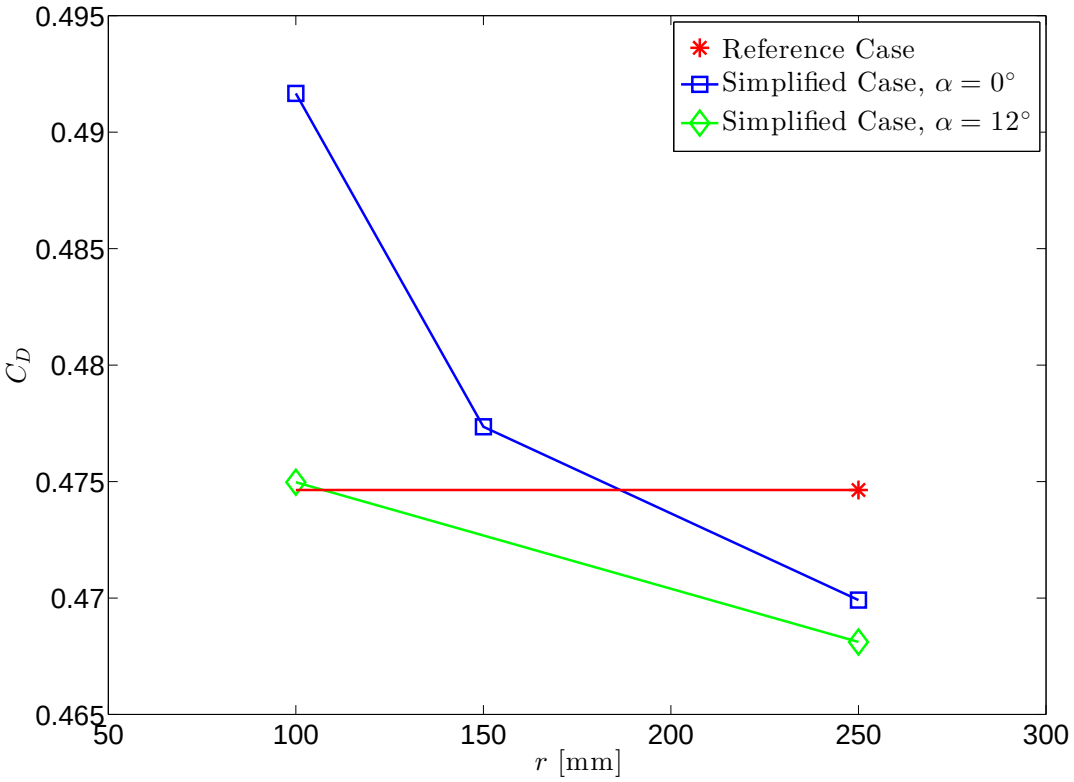

Figure 10.14: Reference domain. Comparison of C_D between the reference case and the simplified cases. The simplified cases are for both α_0 and α_{12} with r between 100–250 mm.

Figure 10.15 shows the accumulated C_D plotted against the longitudinal position.

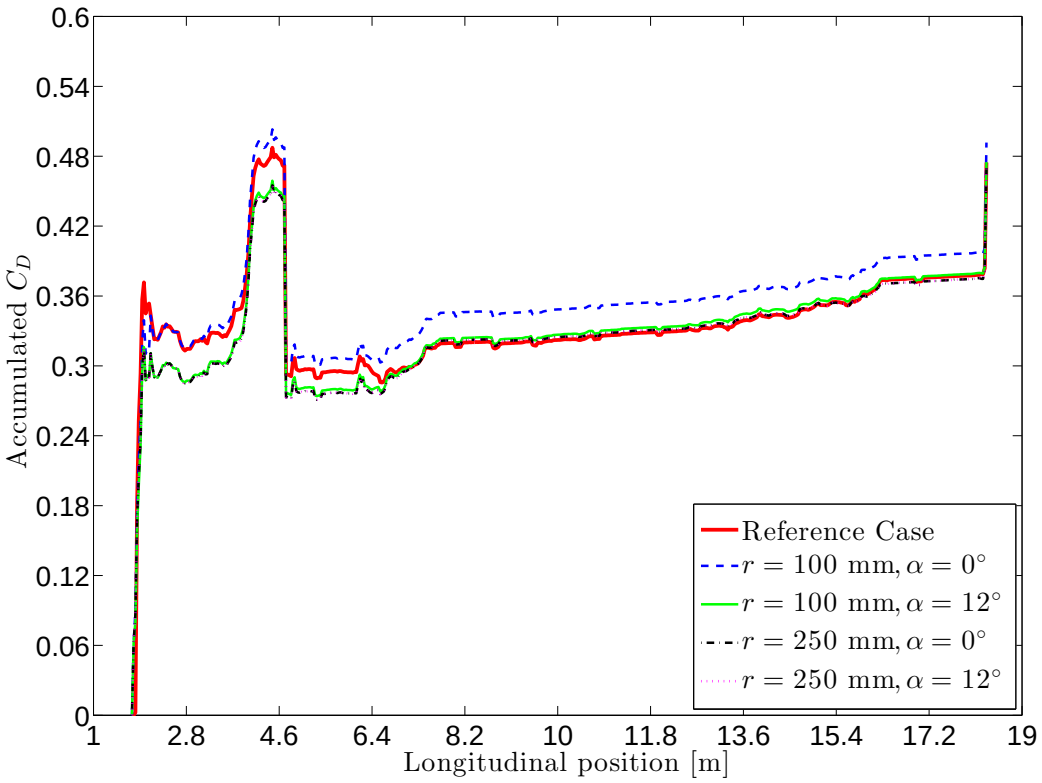

Figure 10.15: Reference domain. Accumulated C_D in regard to the longitudinal position. Comparison of the reference case and the simplified cases for $r = 100$ mm with α_0, $r = 100$ mm with α_{12}, $r = 250$ mm with α_{12} and $r = 250$ mm with α_0.

The accumulated C_D shows the contribution to C_D at different longitudinal positions. As mentioned in section 10.1.1, the original lower front in the reference domain is located at X= 1.81 m and the simplified lower front is translated forward a few mm.

In Figure 10.15, the reference case is compared with the simplified cases for $r = 100$ mm with α_0, $r = 100$ mm with α_{12}, $r = 250$ mm with α_{12} and $r = 250$ mm with α_0. The comparison shows that the simplified case with $r = 100$ mm and α_0 results in an overall higher C_D, which is consistent with the results in Figure 10.14.

The first peaks of the accumulated C_D in Figure 10.15 are shown in a detailed view in Figure 10.16.

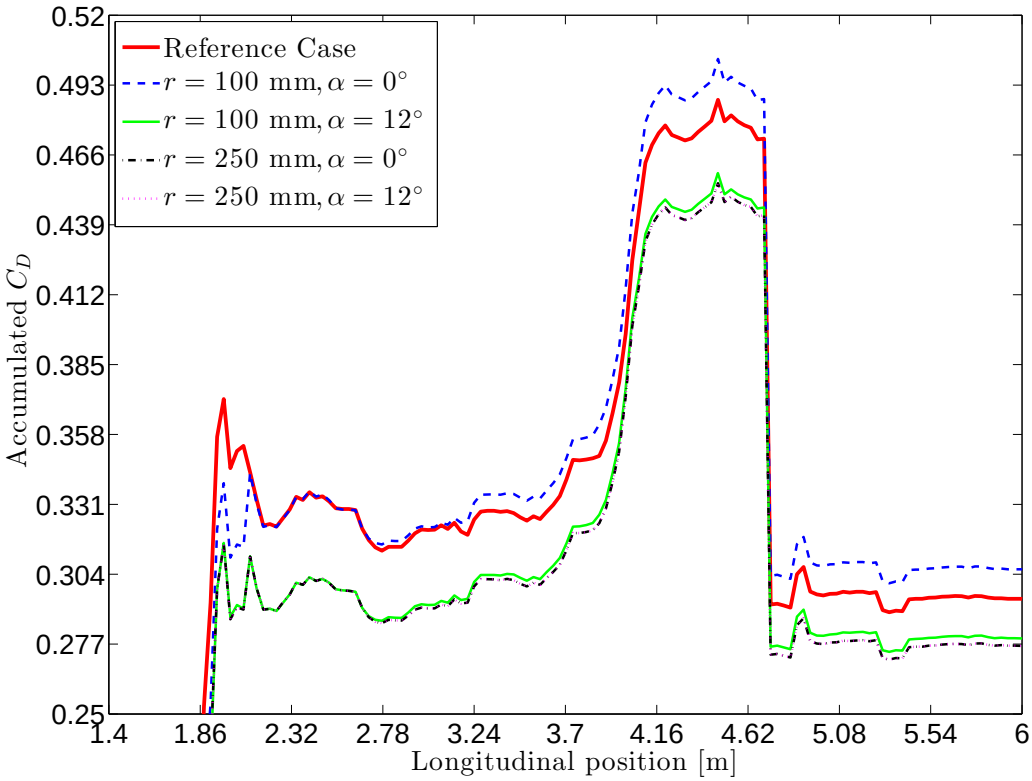

Figure 10.16: Reference domain. A detailed view of the first peaks in Figure 10.15.

Locally, the reference case has the highest accumulated C_D at X = 1.88 m, but regains the most around the front corners. After X = 2.78 m the simplified case with $r = 100$ mm and α_0 has the highest accumulated C_D. For X = 3.1 m there is a deviation in the behavior of the accumulated C_D between the simplified cases and the reference case. This is due to the changed flow through the front which affects how the flow hits the front wheel axle. In the simplified cases the pressure is higher at the front wheel axle, which causes C_D to increase more in this region compared to the reference case.

Another interesting aspect of Figure 10.15 is the different behaviors of the accumulated C_D between the reference case and the simplified cases around X= 6.4 m. This area is shown in a detailed view in Figure 10.17.

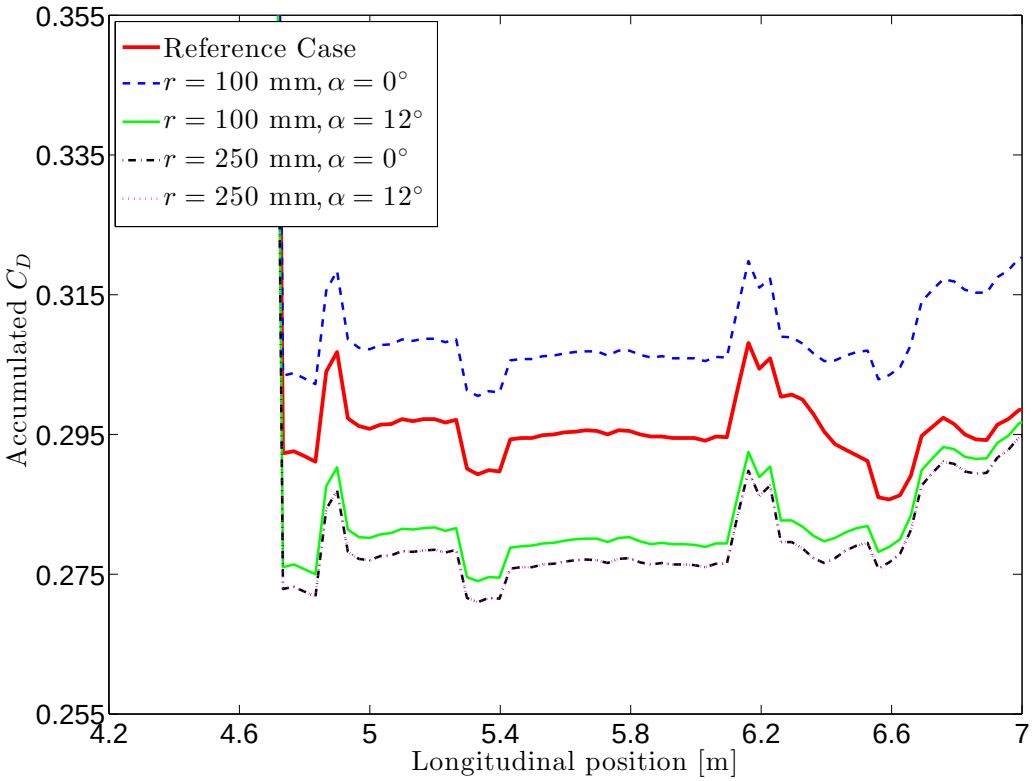

Figure 10.17: Reference domain. A detailed view of accumulated C_D around X= 6.4 in Figure 10.15.

Here it can be seen that the reference case has a larger regain of accumulated C_D than the simplified cases in this area. A closer investigation of the lager regain of the accumulated C_D for the reference case is found in Figure 10.18. It was found that the regain occurred around the rear wheels. Figure 10.18 shows both velocity magnitude and C_p around this area.

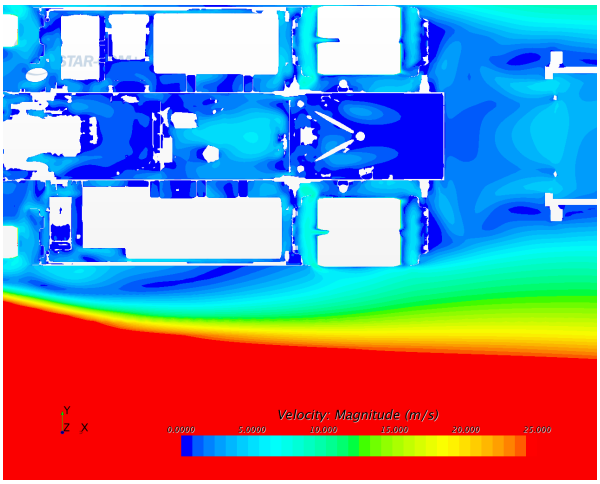

(a) Simplified case; α_{12} and $r = 250$ mm. Bottom view of velocity magnitude on a X-Y plane.

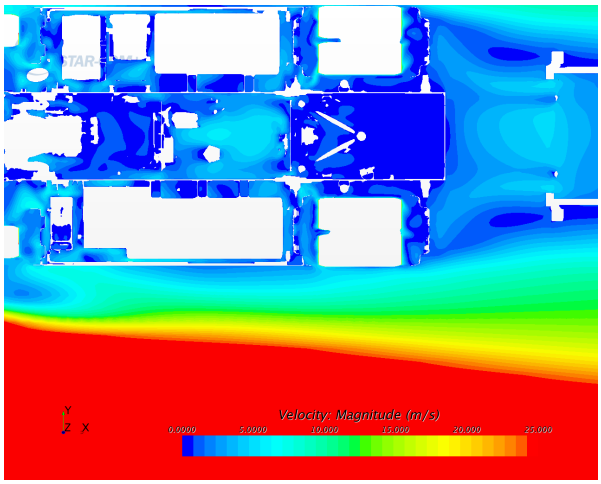

(b) Reference case. Bottom view of velocity magnitude on a X-Y plane.

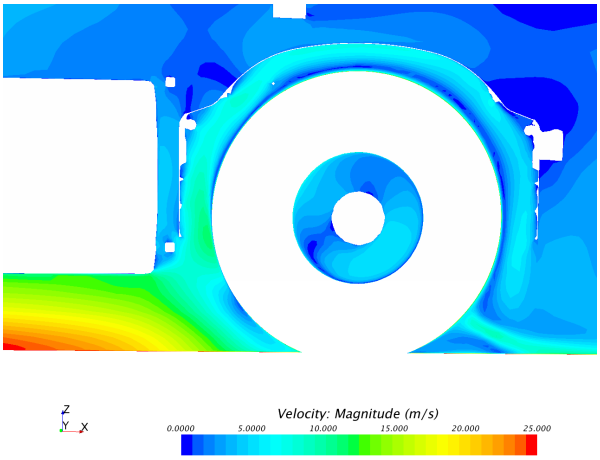

(c) Simplified case; α_{12} and $r = 250$ mm. LHS view of velocity magnitude on a X-Z plane.

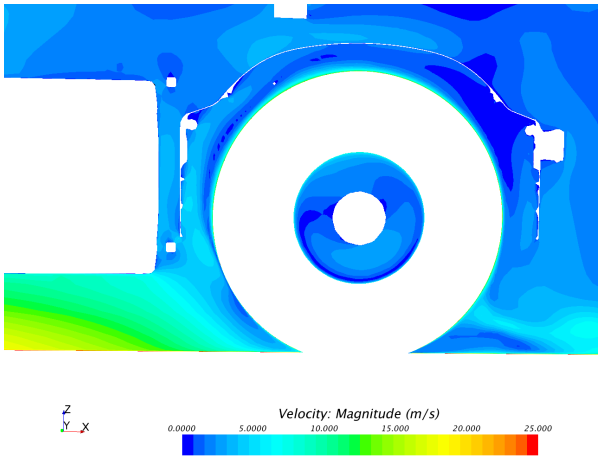

(d) Reference case. LHS view of the velocity magnitude on a X-Z plane.

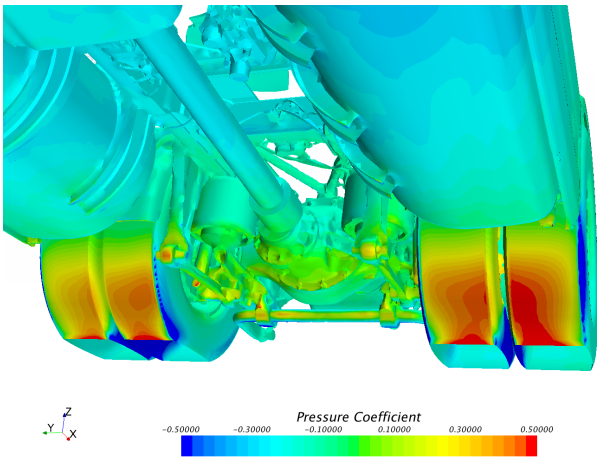

(e) Simplified case; α_{12} and $r = 250$ mm. Bottom perspective view of C_p on the rear wheels.

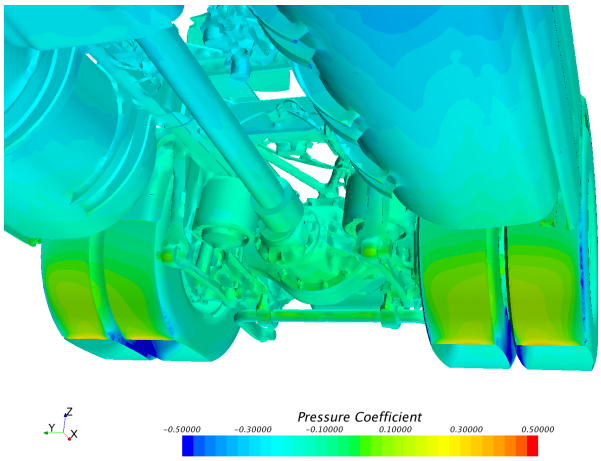

(f) Reference case. Bottom perspective view of C_p on the rear wheels.

Figure 10.18: Comparison of velocity magnitude and C_p around the rear wheels.

From Figure 10.18a it seems that the wake created by the simplified front affects the flow around the rear wheels, see Figure 10.18c. Note the differences compared to Figure 10.18b and Figure 10.18d. The wake due to the simplified front causes higher pressure around the rear wheels for the simplified cases, see Figure 10.18f, compared to the reference case in Figure 10.18e. The higher pressure in turn leads to a smaller regain in accumulated C_D in this area. This explains why the curves for the simplified cases does not decrease as much as the reference cases around X= 6.4.

10.4.2 Velocity Field

Figure 10.19 shows the velocity magnitude and direction on the X-Y plane at Z= 0.31 m for the reference case and the simplified cases with α_0.

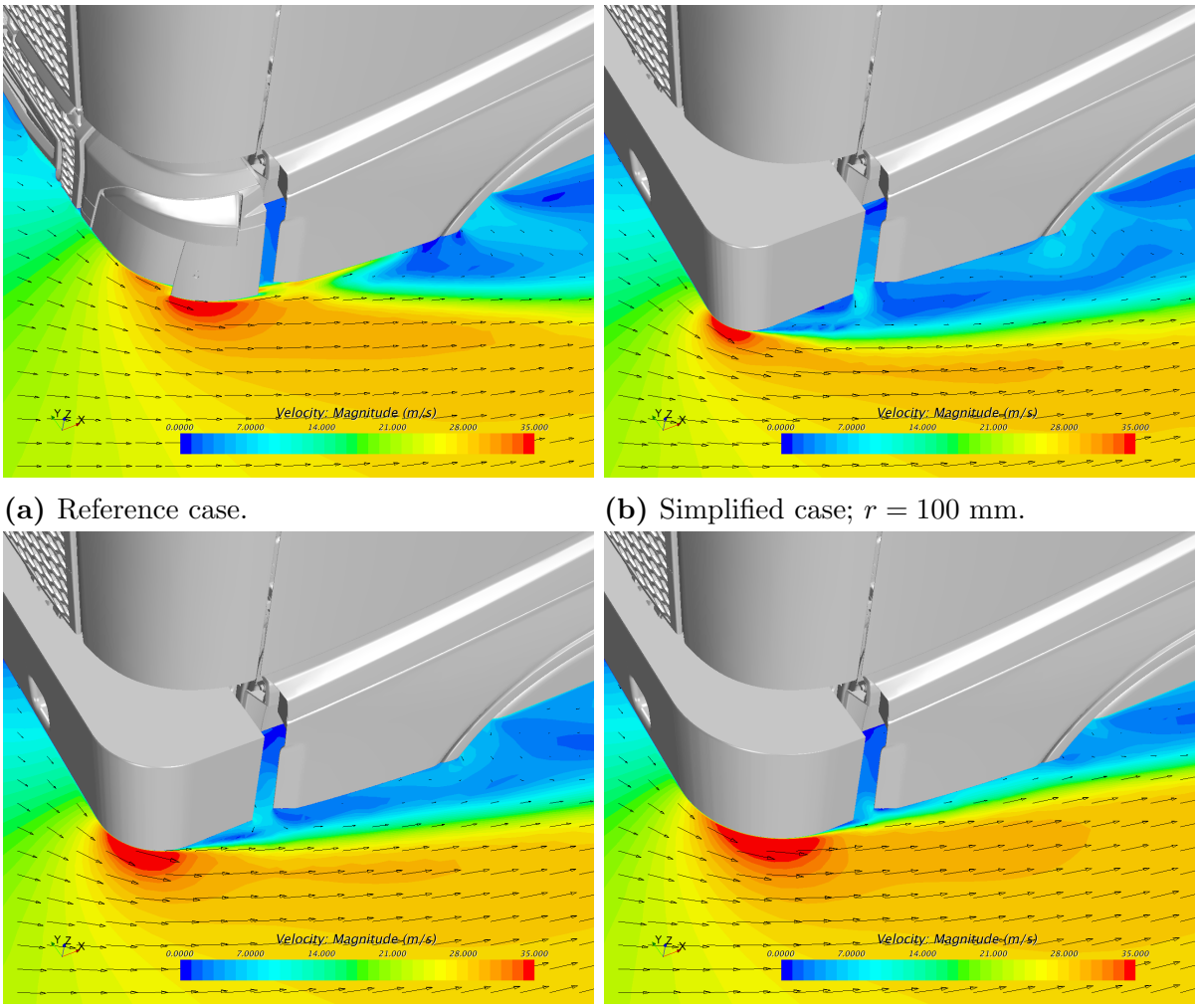

(a) Reference case.

(b) Simplified case; $r = 100$ mm.

(c) Simplified case; $r = 150$ mm.

(d) Simplified case; $r = 250$ mm.

Figure 10.19: Reference domain. Comparison of velocity magnitude and direction between the reference case and the simplified cases with α_0.

From Figure 10.19 it is seen that the flow accelerate around the corner until it reaches the corner crest. After the corner crest a positive LSPG occurs, causing the flow to decelerate and eventually separate.

In all the cases in Figure 10.19, the separation occurs before the end of the corner arc. As in the simplified domain the flow separation occurs earlier for smaller r.

10.4.3 Local Streamwise Pressure Gradient

Calculations of the LSPG were done for the same cases as the velocity magnitude and direction in section 10.4.2. The results are presented in Figure 10.20.

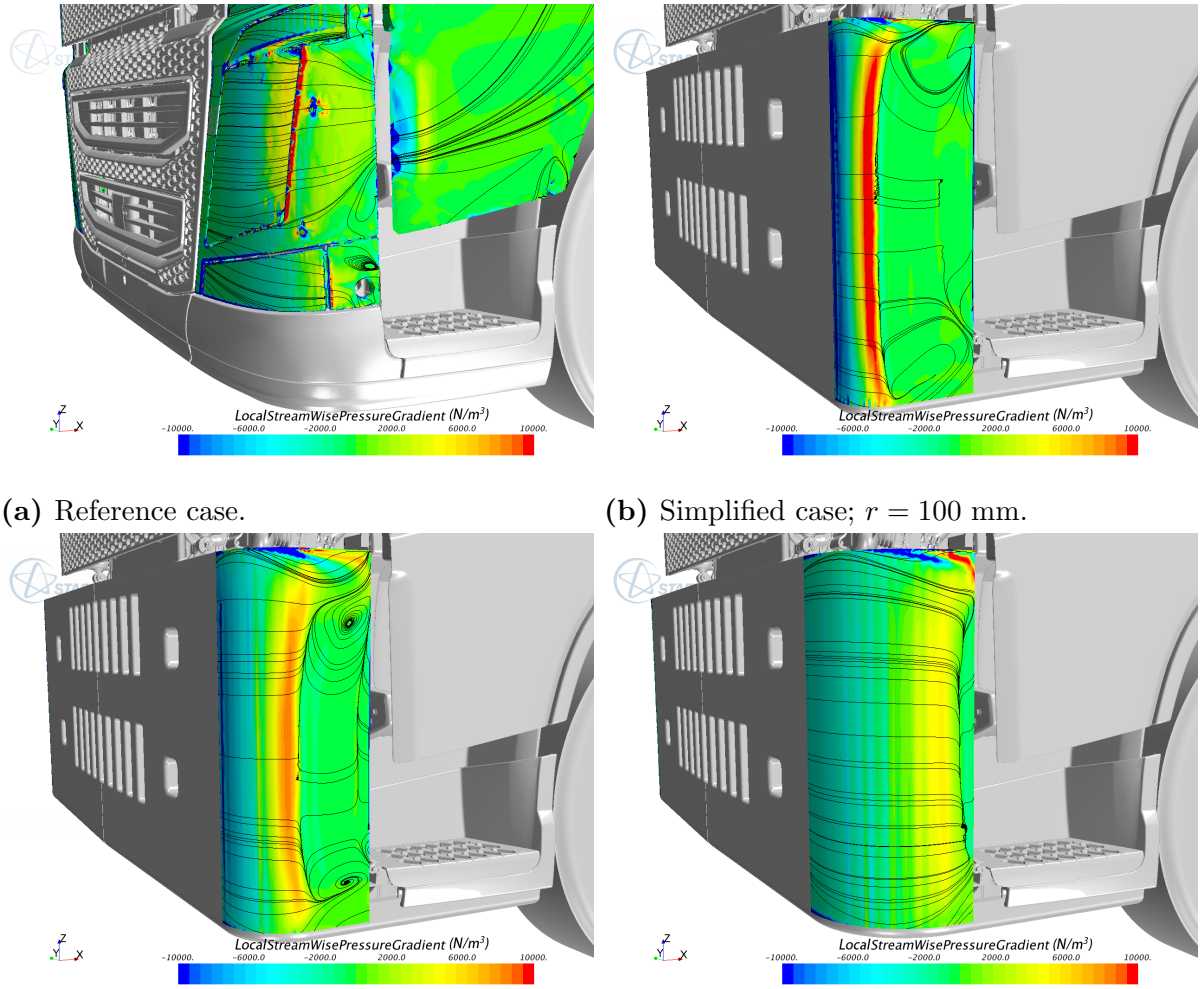

(a) Reference case.

(b) Simplified case; $r = 100$ mm.

(c) Simplified case; $r = 150$ mm.

(d) Simplified case; $r = 250$ mm.

Figure 10.20: Reference domain. Comparison of LSPG between the reference case and the simplified cases with α_0.

For a smaller r the LSPG changes sign from negative to positive earlier as well as the flow separates earlier. The maximum value of the LSPG is higher for smaller r and the transitions are faster. These statements are connected to the geometry. Consequently, the transitions are faster in Figure 10.20b compared to the smooth transitions in Figure 10.19d.

Compare the original lower front and the simplified lower front with $r = 250$ mm and α_0, Figure 10.20a and Figure 10.20d.

Overall, throughout the entire height of the lower front, the streamlines follow the surface better in the simplified case even though it is for α_0. However, in the reference case the streamlines in the middle region follow the surface until the gap. This is possibly due to the air duct, located between the lens and the headlamp panel, which allows air flow through the headlamp.

11 Discussion

This section contains the discussion of the results. The results are set against the objectives and requirements. It also includes advantages and disadvantages of the simplified model and the validity of the results.

11.1 Reference Case

The reference model is highly complex involving many details. The CAD model of the truck is an accurate description of reality. The physics of the turbulent flow is approximated using k–ε model with realizable coefficient. It is difficult to predict an accurate absolute value of C_D using CFD. However, it is not the absolute value which is of importance in this study, it is how the geometrical features and y^+ affect C_D.

To visualize the behavior of the flow and identify the flow separation, a plane with the velocity field was used, but for the reference case it is difficult to study the results only at a given height, since the geometrical features vary. The iso surface in Figure 10.3 illustrates the complexity of the flow separation.

11.2 Simplified Model

By removing details of the lower front the flow will be affected, but by removing them the assumption was that the behavior of the flow and the flow separation caused by α, r and y^+ would be more apparent. The decision to make the corner as a perfect circular arc was made to be able to vary only one parameter to obtain different sharpness. For the reference case α varies at different heights between approximately 10° and 12°. The reason to simplify this to one constant α for all heights was, similarly as with the case of r, to obtain one simple parameter to vary.

An effect of varying r on the simplified lower front is that l_s becomes longer for smaller r. This is the direct consequence of the straight lines being tangential to the circular arc. One other option would be to have discontinues between the lines and the circle, this was regarded as a poor solution since those edges would trigger the flow to separate there. By letting l_s vary, the flow out of the gap will be affected. Furthermore, due to the angled geometry l_s is longer for α_{12} compared to α_0 for the same r, which can be seen in Figure 8.2.

Note that the percentage difference of l_s is less when changing r between 100 mm and 150 mm compared to changing r between 250 mm to 300 mm. Since l_s is overall longer for α_{12} the percentage difference of l_s is overall less when changing r.

The most forward point of the simplified lower front is moved forward a few mm, hence l_s is longer than corresponding distance for the reference case.

A major design decision was the size and the quantities of the holes in the front. The aim was to achieve the right amount of flow through the front. This was done by comparing three different parameters, see Table 8.1.

The first thing that comes to mind is that 40% is a huge difference. This can be explained by the fact that a representative value of the flow out of the gap in the reference case was difficult to obtain. Among other the footstep causes a complex path for the air in the lower region, which has a great impact on the flow through the gap. To get a value that was possible to compare with the simplified domain, where the size of the gap is the same at all heights, an attempt of averaging the flow out of the gap in the reference case was done. This parameter together with the flow around the corner are the most important parameters, but due to the imprecise nature of this value little effort was put into minimizing the deviation in comparison to the other two parameters.

The maximum velocity was compared at a chosen height, hence the simplified lower front was designed to have a flow around the front corner that corresponds to the reference case at that height. Since details, such as side turn indicators, have been removed comparisons were done at a height between the bumper and the side turn indicator, where the corner radius of the reference is fairly constant. The maximum velocity differed almost 8% which was considered small enough.

The mass flow through the cooling package was the parameter most straight forward to analyze and adjust. The final deviation was obtained to around 6%.

The adjustment of the flow is a multi-variable optimization problem. By minimizing one parameter the other two are affected. Hence, to obtain an optimal combination would require a lot of effort and was not considered a priority, therefore a good enough solution were accepted.

The obtained simplified model corresponds well to the requirements. By using α_0 significant flow separation was obtained in both domains and could be investigated for varying r. Even though it was of secondary importance to have a simplification very similar to the reference model, it would have been preferred. For example when decreasing r, l_s increases. In a simplification more similar to the reference model this distance would have been kept constant. With this simplification a smaller r would appear closer to the gap and maybe cause significant flow seperation for α_{12} as well.

The flow deviates more from the wall if the separation occurs earlier at the corner. Hence, if there is an early separation the velocities in the separation bubble will be lower. This results in a lower pressure in the separated region, which makes it easier for the air to flow through the gap.

When there is no flow separation at the corner and l_s is long enough for the flow to straighten up after the corner arc and before the gap, the flow will act as an obstacle giving low flow out of the gap. Hence, when l_s decreases the flow out of the gap increases and the velocities close to the wall behind the gap becomes lower, see Figure 10.7a and Figure 10.7b. In the second figure l_s is shorter, which increases the flow out of the gap and reduces the longitudinal flow close to the wall before the gap. Thus, less flow is pulled along the wall causing lower velocities in the separation bubble close the the wall. Less flow out of the gap is a result of higher pressure by the gap which is obtained for a longer l_s.

11.3 Drag Coefficient

Since drag is a large contributor to fuel consumption it is important to evaluate C_D. When r increases for the cases with α_0, C_D rapidly decreases until $r = 200$ mm, see Figure 10.5.

If the flow has not already separated before the gap it will separate there. For $r < 200$ mm less flow separation occurs with increased r. Above $r = 200$ mm almost no flow separation occurs before the gap. This is seen from the streamlines in Figure 10.9 and Figure 10.10.

Minimums of C_D can be found for both α_{12} and α_0, which occur when there is no significant flow separation at the corner. When there is almost no flow separation at the corner a shorter l_s gives a higher C_D. This since the shorter l_s gives a lower pressure by the gap which results in a greater difference in pressure between the front and the gap. A decrease in l_s does not linearly increase C_D. The percentage difference of decreasing l_s is higher for a shorter l_s, which affect C_D. This is seen in the curves in Figure10.5, where the increase in C_D is greater for r between 250 mm and 300 mm than r between 200mm and 250 mm.

Varying r has less impact with α_{12} since the corner is 78° compared to 90°, thus the flow with α_{12} has to turn less, which requires less energy. Since the flow, for almost all α_{12} cases, contains enough energy the flow follows the surface without separating. For α_{12} flow separation is only found for $r < 100$ mm with y^+_{low}. Another reason for the less impact of varying r is due to the overall longer l_s.

When there is almost no flow separation at the corner, α_{12} contributes to a higher C_D compared to α_0. This is due to the angled geometry which causes the streamlines to deviate from the longitudinal direction. The deviation allows more flow out of the gap and the effects on C_D and the velocities in the separation bubble are similar as for a short l_s, but greater. For $y^+_{low,c}$ this effect is seen in Figure 10.5 where α_0 and α_{12} intersects for r between 200 mm and 250 mm. At $r = 250$ mm the C_D value of α_{12} is the higher one. The same effect can be seen for y^+_{high} for $r = 150$ mm.

Considering the simplified cases, i.e. the simplified lower front in the reference domain, it can be seen from Figure 10.14 that both simplified cases, α_0 and α_{12}, with $r = 250$ mm have lower C_D than the reference case. It is probably due to fewer edges. This was expected and discussed in section 11.2. The difference in C_D between the reference case and the simplified case with $r = 250$ mm and α_0 was around 1%, which is considered quite small. Since the flow separates at the corner for all considered simplified cases it is natural that α_{12} has lower C_D.

11.4 Local Streamwise Pressure Gradient

As stated in section 4.4 the flow separation for the two-dimensional case occurs when $\tau_w = 0$. The LSPG (in that case dp/dx_n) is easily related to the flow separation, since it is proportional to the derivative of τ_w. This simple relation is not true for the three-dimensional case, since there is a lateral direction affecting.

Since it was desirable to find a connection between LSPG and flow separation for the three-dimensional case a lot of focus has been put on generating and analyzing LSPG.

It has been found that when r increases the maximum LSPG value is lower, occurs later and the transitions are smoother for both y^+_{low} and y^+_{high}. It has also been found that flow separation is not connected to a specific maximum value of LSPG. This can be seen from Figure 10.9e where the flow separates after encountering a LSPG of around 10^4 N/m^3, but in Figure 10.9a the flow does not separates until after encountering a LSPG of above 2.1×10^4 N/m^3.

By comparing subfigures in e.g. Figure 10.9, it seems that separation is connected to the positive second derivate of the streamwise pressure. This correspond to the theory in 4.3, which states that a too great increase of the pressure rate will lead to flow separation.

In Figure 10.10a the LSPG goes from 0 N/m^3 to 10^4 N/m^3 in a shorter distance than the LSPG in Figure 10.10c goes from 0 N/m^3 to 8×10^3 N/m^3. For the last case mentioned the change is less for a longer distance and separates less. For an even lower gradient the flow does not separate.

For all results of the LSPG in the simplified domain there is a deviation in the upper region. This deviation is likely due to the symmetry boundary condition. This since no flow can pass through this boundary, hence resulting in a nearly two-dimensional flow at the boundary. Compare this with the lower region where the streamlines somewhat turns downwards. A more representative result might have been achieved by expanding the domain upwards and hence moving the boundary, which forces the flow to move parallel, away from the investigation area.

Note that the values are for the simplified domain. In the reference domain, however, the flow separates easier. Here the flow separates for a LSPG which goes from 0 N/m^3 to 6×10^3 N/m^3 in a similar distance as the simplified domain case with α_0 and $r = 250$ mm, compare Figure 10.20d and 10.10c. This can be explained by the complexity of the reference domain, such as the complexity of the gap by the footstep and the rotating wheels.

11.5 Comparison of Different y^+ Distribution

The absolute value of C_D changes when the mesh resolution is changed, until the mesh is fine enough to solve the flow completely. Therefore, it is important to investigate the impact of different mesh density on C_D.

In Figure 10.13 y^+ is the average of the entire surface of the front corner (from the beginning of the corner arc to the gap). The distributions of y^+ where from the averages are taken is shown in Figure 10.12. It would have been more accurate to take the average of the surface of only the corner arc, which would have resulted in a lower average of y^+.

It is likely that the mesh with the averaged $y^+ \approx 1$ gives the most accurate results. When using CFD, meshes of either $y^+ \approx 1$ or $y^+ \approx 30-100$ are common practice. Meshes having $5 < y^+ < 30$ should generate poor accuracy. One reason is that these meshes are not fine enough to completely resolve the flow. Another reason is that since the first cell is located in the buffer region wall functions works poorly. However, all-y^+ wall treatment should give somewhat better accuracy for meshes of $5 < y^+ < 30$, since it mixes low-y^+ and high-y^+ wall treatments.

The highest C_D curve in Figure 10.13 was obtained with the averaged $y^+ \approx 2$, which is very similar to the C_D curve obtained with the averaged $y^+ \approx 1$. Thus, it seems that STAR-CCM+ solves the flow equations around the front corners using mainly low-y^+ wall treatment for low values of y^+.

By further studying the curves in Figure 10.13 it can be seen that the separation point is delayed by poor resolution which gives a lower C_D. The difference in C_D between $y^+ \approx 1-2$ and $y^+ \approx 6-30$ is nearly constant for $r \leq 150$ mm. The difference between these two groups of curves deviates slightly since the separation point occurs at different locations of the front corner throughout the height.

Therefore, a minor delay of the flow separation may cause significant change in C_D. The effect is seen in Figure 10.13, where the C_D values for $r \leq 150$ mm obtained with $y^+ \approx 60$ deviate from those obtained with $y^+ \approx 1$. In addition, it can be seen that for $r \geq 150$ mm the C_D curve obtained with $y^+ \approx 30$ is lower than $y^+ \approx 60$.

Looking at $r \leq 150$ mm and using $y^+ \approx 1$ curve as a reference, meshes having $5 < y^+ < 30$ compared to $y^+ \approx 60$ gave more accurate results with a significantly higher C_D. This is because the separation point is delayed with $y^+ \approx 60$ for such small r. The same trend is seen in Figure 8.8, where a mesh with $y^+ \approx 30 - 100$ did not predict any separation at the lower edge. This gave a C_D which was 200 drag counts lower than obtained with $y^+ \approx 1$, where separation was predicted.

From these results the use of all-y^+ wall treatment seems to work quite well. It is not crucial to have meshes of either $y^+ \approx 1$ or $y^+ \approx 30 - 100$ but meshes in the intermediate region works as well. However, for small r where flow separation occurs it is important to have sufficient resolution in wall-normal direction.

12 Conclusion

The behavior of the flow separation affected by the different geometrical features: front corner radii, r, and draft angle, α has been investigated. The mesh density, here measured as y^+, has also been investigated. By removing the details of the lower front the behavior of the flow and the flow separation caused by α, r and y^+ was more apparent. As discussed in section 11.1 it is not the absolute values which are of importance in this study, it is how y^+ and the geometrical features affect the C_D.

There were two main requirements when designing the simplified model. The first one was that the geometry and flow situation should be similar to the reference case. The second requirement was that r should be adjustable between 100–300 mm.

The design process of simplifying the lower front was carried out in the simplified domain with $r = 250$ mm and α_{12}, and compared with the reference case. Note that the reference case resides in the reference domain. To achieve the right amount of mass flow through the simplified lower front, the parameters in Table 8.1 were evaluated. The average velocity out of the gap differed 40%, the maximum velocity around the front corner differed almost 8% and the mass flow through the CAC differed around 6%. These values were considered small enough. To obtain an optimal combination would require a lot of effort and was not considered a priority, therefore a good enough solution were accepted.

The simplified lower front model with α_{12} corresponded well to the geometry requirement, but did not result in significant flow separation before the gap in the simplified domain, even for small values of r. Since the main purpose was to investigate flow separation for varying r using α_0 was motivated, which resulted in significant flow separation at the corner for varying r.

If there is an early flow separation, the separation will be larger and the deviated flow will enable more flow out of the gap, due to the low pressure.

When there is no flow separation at the corner the distance between the end of the corner arc and the gap, l_s, affects C_D. For a short l_s there is not enough space for the flow to straighten up fully before the gap and therefore some of the flow close to the wall is in lateral direction when reached the gap. Hence, there is a lower pressure in the region by the gap allowing more flow out of the it. The lower pressure by the gap increases C_D. The higher mass flow out of the gap along with the less longitudinal directed flow reduced the velocities close to the wall in the separation bubble behind the gap.

Due to the angled geometry l_s is longer for α_{12} than α_0 for the same r. To avoid impact on C_D caused by varying l_s a preferred model would either keep l_s constant for varying r and α.

Varying r has less impact on α_{12} compared to α_0. This is since almost no flow separation occurs at the corner for α_{12}, which is due to the a smaller turn, and since l_s is overall longer for α_{12}.

α_{12} causes a flow deviation from longitudinal direction which in turn causes a lower pressure between the deviated flow and the gap opening compared to α_0. The lower pressure allows more flow out of the gap and the effects on C_D and the velocities in the separation bubble are similar as for a short l_s, but greater.

Regarding mesh density in wall-normal direction, it is likely that $y^+ \approx 1$ gives the most accurate results. The hypothesis was that there would be no significant difference in the results for $y^+ \approx 30 - 100$. This has been shown not to be true in regions of small r where flow separation occurs. For r smaller than 150 mm it was shown that the results deviated significant for the mesh of $y^+ \approx 30$ compared to the mesh of $y^+ \approx 60$, since poor accuracy delays the separation point.

The use of all-y^+ wall treatment seemed to work quite well. Hence, it is not crucial to have meshes of either $y^+ \approx 1$ or $y^+ \approx 30 - 100$ but meshes in the intermediate region works as well. However, for small r where flow separation occurs it is important to have sufficient resolution in wall-normal direction. Therefore, it is recommended to have a resolution of $y^+ \approx 1$ for the roof deflectors, side deflectors and rearview mirrors etc.

Based on the discussion in section 11.3, when a sharp corner is followed by a α the flow does not separate as easily.

The conclusion about the dependence of LSPG and flow separation is difficult to draw from these results. To obtain a relation between the LSPG and flow separation it might be beneficial to study X-Y plots of normalized LSPG and/or C_p. This has not been done due to time constraints. However, it has been found that flow separation is not connected to a maximum value of LSPG, but it seems to be connected to the positive derivative of LSPG.

13 Future Work

Since flow separation due to the front corner is relatively unexplored at Volvo GTT, a simplified environment in a small domain was used to isolate the behavior. The top surface of the small domain was developed to flush the top of the simplified lower front. The boundary condition of the top surface was set to symmetry plane. This affected the behavior in the upper region and a recommendation is to extend the small domain upwards to get rid of this impact.

A suggestion to continue this work is to further study the connection between the rate increase of pressure and the flow separation point. As mentioned in section 12 it might be beneficial to study X-Y plots of the normalized LSPG and/or C_p.

In this investigation the gap affected the results significant. When l_s was decreased a trend of increasing C_D was found, see Figure 10.5. Therefore, when investigating flow separation around the front corners, next step should be to close this gap. If this gap is closed one could expect that for larger r, where no flow separation at the corner occurs, the C_D curves will flatten out. Moreover, a study of how the gap size impacts the overall flow and drag would be interesting as well as continue to investigate α to find an optimal combination (giving as low C_D as possible) of α, r and gap size.

Another thing to do is to change the geometry. For instance, increase the radius of the lower edge to be able to use a finer mesh ($y^+ \approx 1$) everywhere, without giving rise to unwanted flow separations. In this investigation, $y^+ \approx 30 - 100$ was used everywhere except at the front corners.

An investigation to verify the mesh in wall-parallel direction would be an interesting thing to do, since the mesh study in this thesis was only carried out for all radii in wall-normal direction.

It would also be interesting to investigate how the flow separation behaves around the front corners and how the separation point is affected when the flow is unsteady. The transient effects could be considered by using for instance Detached Eddy Simulation (DES).

Bibliography

[1] Frank M. White. *Fluid mechanics*. McGraw-Hill Higher Education, New York, 7th ed. edition.

[2] James R. Welty. *Fundamentals of momentum, heat, and mass transfer*. Wiley, Hoboken, N.J. ; Chichester, 5th ed. / james r. welty et. al. edition.

[3] Lars Davidson. Fluid mechanics, turbulent flow and turbulence modeling, lecture notes in msc courses. Technical report, 2010. 250.

[4] S. B. Pope. *Turbulent flows*. Cambridge University Press, Cambridge.

[5] Hermann Schlichting and K. Gersten. *Boundary-layer theory*. Springer, Berlin; London, 8th rev. and enl. ed. edition.

[6] R. H. Barnard. *Road vehicle aerodynamic design : an introduction*. Longman, Harlow.

[7] Bruce R. Munson, Donald F. Young, and Theodore H. Okiishi. *Fundamentals of fluid mechanics*. Wiley, New York ; Chichester, 4th ed. edition, 2001. ISBN 047144250X.

[8] Frank P. Incopera and David P. Dewitt. *Fundamentals of Heat and Mass Transfer*. Wiley, New York; Chinchester, 4th ed. edition.

[9] P. W. Bearman. On vortex shedding from a circular cylinder in the critical reynolds number regime. *Journal of Fluid Mechanics*, 37:577–585, 7 1969. ISSN 1469-7645. doi: 10.1017/S0022112069000735. URL `http://journals.cambridge.org/article_S0022112069000735`.

[10] Wolf-Heinrich Hucho and Syed R. Ahmed. *Aerodynamics of road vehicles : from fluid mechanics to vehicle engineering*. Society of Automotive Engineers, Warrendale, Pa., 4th ed. edition.

[11] CD-adapco. Star-ccm+, 2014. URL `http://www.cd-adapco.com/products/star-ccm`. Accessed: 2014-09-21.

[12] Andreas Sveningsson and Lars Davidson. Assessment of realizability constraints in v2f turbulence models. *International Journal of Heat and Fluid Flow*, 25:785–794, 2004. ISSN 0142-727X.

[13] P. A. Durbin. On the k - ϵ 3 stagnation point anomaly. *International Journal of Heat and Fluid Flow*, (17):89–90, 1996.

Appendices

A Settings for the Simplified Domain in STAR-CCM+

Table A.1: General mesh settings for the simplified domain.

Setting		Value [mm]
Base size		32
Prism layer thickness		16
Large refinement box	Isotropic size	16
Small refinement box	Isotropic size	8

Table A.2: Mesh Settings for the parts in the simplified domain.

Part name	Surface min size [mm]	Surface target size [mm]	No. of prism layers	Prism layer stretching
Bumper	2	4	10	1.15
CAC sides	16	32	1	1.5
CAC inlet and outlet	8	8	1	1.5
Front corners	2	8		1.175
Remaining lower front	2	32	10	1.1
Small box	16	32	10	1.1

Table A.3: Sizes of the small domain and the refinement boxes.

Small domain (box)	65 m x30 m x 0.65 m
Small refinement box	2.4 m x 2.5 m x 0.6 m
Large refinement box	4.3 m x 3.3 m 0.68 m

Table A.4: Physical models used in the simplified domain.

Setting	Value
Space	Three-dimensional
Motion	Stationary
Time	Steady
Material	Gas – air
Flow	Segregated flow
Equation of state	Constant density
Viscous regime	Turbulence
Turbulence model	RANS – standard k–ε with realizable coefficient
Wall treatment	Two-layer all y^+

Table A.5: Boundary conditions used in the simplified domain.

Setting		Value
All part surfaces Domain sides and	Stationary wall Symmetry planes	No-slip
Top		
Ground	Stationary wall	No-slip
Inlet	Velocity inlet Turbulence intensity Turbulent viscosity ratio	25 [m/s] 0.002 200
Outlet	Pressure outlet Turbulence intensity Turbulent viscosity ratio Back flow direction	0 [Pa] 0.01 10 Boundary-normal

B Simplified Model

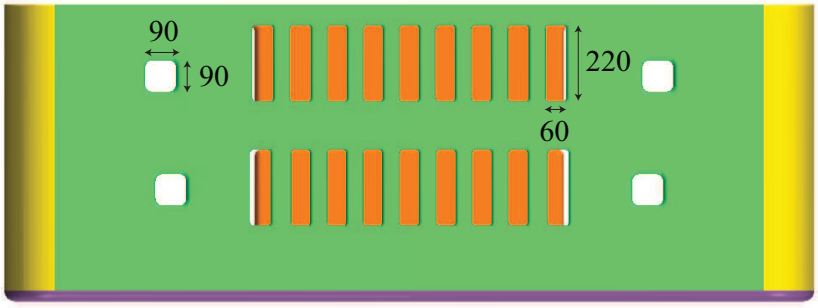

Figure B.1: Dimensions of the holes in the simplified lower front. The dimensions are given in mm.

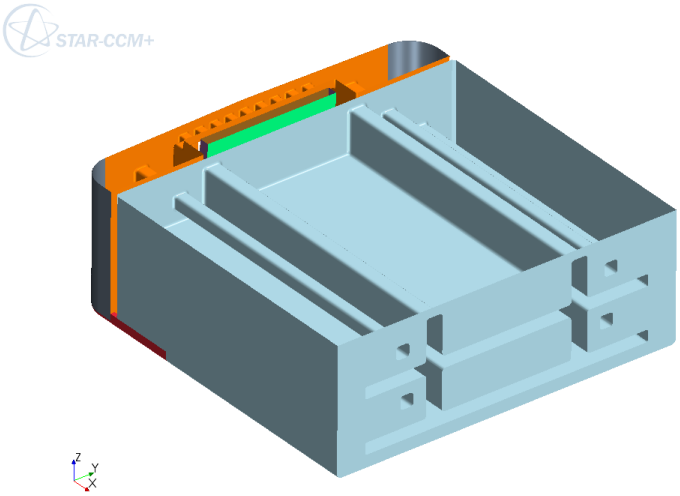

Figure B.2: Simplified domain. The holes through the small box is visualized.

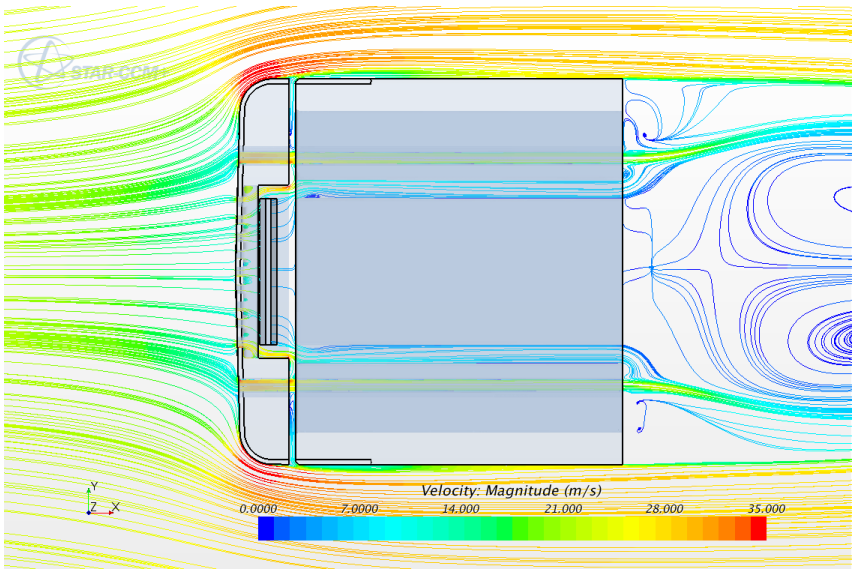

Figure B.3: Simplified domain. Streamlines visualizing the flow through: the front (7.5 kg/s), the small box (5.7 kg/s) and out of the gap (0.8 kg/s). The remaining flow (1 kg/s) goes through the lower gap.